ORIGINAL ARTICLE

Basal Gp78-dependent mitophagy promotes mitochondrial health and limits mitochondrial ROS

Parsa Alan[1] · Kurt R. Vandevoorde[1] · Bharat Joshi[1] · Ben Cardoen[2] · Guang Gao[1] · Yahya Mohammadzadeh[1] · Ghassan Hamarneh[2] · Ivan R. Nabi[1]

Abstract

Mitochondria are major sources of cytotoxic reactive oxygen species (ROS), such as superoxide and hydrogen peroxide, that when uncontrolled contribute to cancer progression. Maintaining a finely tuned, healthy mitochondrial population is essential for cellular homeostasis and survival. Mitophagy, the selective elimination of mitochondria by autophagy, monitors and maintains mitochondrial health and integrity, eliminating damaged ROS-producing mitochondria. However, mechanisms underlying mitophagic control of mitochondrial homeostasis under basal conditions remain poorly understood. E3 ubiquitin ligase Gp78 is an endoplasmic reticulum membrane protein that induces mitochondrial fission and mitophagy of depolarized mitochondria. Here, we report that CRISPR/Cas9 knockout of Gp78 in HT-1080 fibrosarcoma cells increased mitochondrial volume, elevated ROS production and rendered cells resistant to carbonyl cyanide m-chlorophenyl hydrazone (CCCP)-induced mitophagy. These effects were phenocopied by knockdown of the essential autophagy protein ATG5 in wild-type HT-1080 cells. Use of the mito-Keima mitophagy probe confirmed that Gp78 promoted both basal and damage-induced mitophagy. Application of a spot detection algorithm (SPECHT) to GFP-mRFP tandem fluorescent-tagged LC3 (tfLC3)-positive autophagosomes reported elevated autophagosomal maturation in wild-type HT-1080 cells relative to Gp78 knockout cells, predominantly in proximity to mitochondria. Mitophagy inhibition by either Gp78 knockout or ATG5 knockdown reduced mitochondrial potential and increased mitochondrial ROS. Live cell analysis of tfLC3 in HT-1080 cells showed the preferential association of autophagosomes with mitochondria of reduced potential. Xenograft tumors of HT-1080 knockout cells show increased labeling for mitochondria and the cell proliferation marker Ki67 and reduced labeling for the TUNEL cell death reporter. Basal Gp78-dependent mitophagic flux is, therefore, selectively associated with reduced potential mitochondria promoting maintenance of a healthy mitochondrial population, limiting ROS production and tumor cell proliferation.

Keywords Gp78 ubiquitin ligase · Mitochondria · Mitophagy · Reactive oxygen species · GFP-mRFP tandem fluorescent-tagged LC3 · Spot detection · SPECHT

Parsa Alan, Kurt R. Vandevoorde, Bharat Joshi and Ben Cardoen equal contributions to this work.

✉ Ivan R. Nabi
irnabi@mail.ubc.ca

[1] Life Sciences Institute, Department of Cellular and Physiological Sciences, School of Biomedical Engineering, University of British Columbia, 2350 Health Sciences Mall, Vancouver, BC V6T 1Z3, Canada

[2] School of Computing Science, Simon Fraser University, Burnaby, BC V5A 1S6, Canada

Introduction

Mitophagy is a process that selectively targets mitochondria for autophagy and lysosomal degradation [1–3]. Mitophagy plays a critical role in cellular health by controlling mitochondrial mass and eliminating damaged or dysfunctional mitochondria [4]. Reactive oxygen species (ROS), such as superoxide or hydrogen peroxide, are generated in mitochondria through oxidative phosphorylation, by membrane-bound NADPH oxidase or by other bioenergetic conditions and are elevated in tumor cells [5–8]. At high levels, ROS induces DNA mutations leading to cellular transformation and tumorigenesis as well

as, above a threshold, to apoptosis and tumor necrosis [9, 10]. Autophagy and, more specifically, mitophagy play key roles in controlling ROS production and thereby cancer progression [11, 12]. Indeed, in response to hypoxia, BNIP3/NIX/FUNDC1-induced mitophagy reduces cellular ROS levels and limits metastasis [2, 13, 14]. However, the relationship between mitophagy and ROS production and its regulation in cancer remains complex and not fully elucidated [15].

Several ubiquitin-dependent molecular pathways mediate mitophagy, including the well-characterized PINK1/Parkin pathway, closely associated with Parkinson's disease [16]. In response to mitochondrial damage, including ROS, loss of mitochondrial potential prevents removal of PTEN-induced putative kinase 1 (PINK1) from the outer mitochondrial membrane; PINK1, through phosphorylation, recruits and activates the Parkin E3 ubiquitin ligase to damaged mitochondria, triggering recruitment of the autophagy machinery, including the autophagosome-associated protein, microtubule-associated protein 1A/1B-light chain 3 (LC3/ATG8), and autophagosome formation [17–20]. Lipidation transforms cytosolic LC3-I to membrane-associated LC3-II-promoting formation of the phagophore that engulfs dysfunctional mitochondria into autophagosomes for delivery to lysosomes for degradation [21]. However, many cell lines do not express Parkin, tissue expression of Parkin is varied, and mitophagy independent of Parkin and/or PINK1 has been reported [22–24]. Despite the focus on the role of PINK1 and Parkin in damage-induced mitophagy [25–28], both are dispensable for basal mitophagy in various in vivo systems [23, 29]. Other molecular mechanisms must, therefore, regulate basal mitophagy.

Other ubiquitin ligases such as Mul1, MARCH, SMURF, HUWE1, RNF185 and Gp78 have been reported to function independently or in parallel with PINK1/Parkin [30–36]. PINK1-dependent, Parkin-independent mitophagy pathways include the synphilin/SIAH1 and the Mulan pathways [32, 33, 37]. However, synphilin is primarily expressed in the brain and whether Mulan functions downstream of or independently of PINK1 remains to be determined [1]. Gp78, a key E3 ubiquitin ligase in the endoplasmic reticulum (ER) [38, 39], exhibits both pro-metastatic and tumor suppressor properties [40, 41]. Upon mitochondrial depolarization, Gp78 degrades mitofusin [34, 42, 43]. Gp78 degradation of outer mitochondrial membrane proteins form mitoplasts that interact with the endoplasmic reticulum and are degraded by reticulophagy [44]. A role for Gp78 in mitophagy is based primarily on loss of mitochondrial mass upon Gp78 overexpression in the presence of the mitochondrial oxidative phosphorylation uncoupler CCCP [34, 42–44]. Defining the role of Gp78, and other mitophagy effectors, in tumor cell mitophagy requires study of Gp78 knockout cells and of basal, and not damage-induced, mitophagy.

Here, using CRISPR/Cas9 knockout of Gp78 in HT-1080 fibrosarcoma cells, Gp78 is shown to promote both basal and damage-induced mitophagy leading to ATG5-dependent reduction in mitochondrial mass, increased mitochondrial potential and reduced mitochondrial ROS. Application of the spot detection algorithm SPECHT [45] to monitor flux of the autophagosome reporter tfLC3 localized autophagosome maturation in proximity to mitochondria with reduced membrane potential. Xenograft tumors of wild-type and Gp78 KO HT-1080 cells recapitulated the mitochondrial phenotype of cells in culture, presenting increased mitochondrial labeling, as well as increased expression of the Ki67 cell proliferation marker and reduced labeling for the TUNEL cell death marker. By targeting damaged mitochondria for degradation, Gp78-dependent mitophagic flux regulates the homeostasis of healthy mitochondria promoting mitochondrial health and reducing ROS production and proliferation of cancer cells.

Results

Impaired basal and damage-induced mitophagy in Gp78 knockout HT-1080 cells

The HT-1080 fibrosarcoma cell line expresses high levels of Gp78 protein and has been extensively used for the study of Gp78 [41, 46, 47]. We previously used stable miRNA and inducible lenti-shRNA approaches to post-transcriptionally knockdown Gp78 mRNA [34, 47–49]. We now applied CRISPR/Cas9 to knockout Gp78 using two different guided RNA sequences: gRNA1 targets and eliminates the ATG start codon; gRNA2 induces a frameshift sixteen amino acids downstream of the ATG start codon (Fig. 1A). Complementary gRNA1 or gRNA2 oligos were annealed and cloned in the GeneArt-OFP plasmid, sequence verified and transfected into HT-1080 cells. We screened 60 clones by Western blotting; from 38 Gp78 knockout clones, three clones showing complete absence of Gp78 from each gRNA were selected (gRNA1: clones #3, 4 and 7; gRNA2: clones #13, 36 and 41). Western blots showed the complete absence of Gp78 in all six gRNA1 and gRNA2 clones compared to wild-type HT-1080 cells (Fig. 1A). Gp78 KO HT-1080 cells showed elevated levels of MFN1 but not of MFN2, DRP1 or OPA-1 (Supp. Figure 1A), consistent with selective Gp78 targeting of MFN1 for proteasomal degradation [43]. No significant differences in expression of the autophagy-related proteins ATG5, p62, ULK1, LC3BI/II or mitophagy specific PINK1 were detected between WT and Gp78 KO HT-1080 cells (Supp. Figure 1B).

Gp78 CRISPR/Cas9 knockout HT-1080 clones labeled for the inner mitochondrial protein ATP synthase subunit β all showed extended mitochondrial networks compared to

Fig. 1 CRISPR/Cas9 knockout of Gp78 in HT-1080 prevents damage-induced mitophagy. **A** Schematic showing Exon 1 region of Gp78 gene on chromosome 16 and location of gRNA1 targeting the start codon, deleting ATG (ΔG or inserting extra T), and of gRNA2, inserting an extra T at amino acid 16 causing frameshift and termination. Western blot for Gp78 is shown for wild-type HT-1080 cells and all six gRNA1 and gRNA2 Gp78 knockout CRISPR clones with β-actin as a loading control (full blots shown in Supp. Figure 5). **B** Wild-type HT-1080 cells and the six Gp78 knockout CRISPR clones were incubated with either DMSO or 10 μM CCCP for 24 h then fixed and labeled for mitochondrial ATP synthase subunit β and imaged by 3D spinning disk confocal microscopy. Representative images of HT-1080 and a CRISPR clone including magnification of boxed region are shown. Quantification of total mitochondrial volume and average volume per mitochondrial segment are shown in the bar graphs ($n = 3$ independent biological replicates; > 10 cells/ condition per experiment; *, $p < 0.05$; **, $p < 0.01$; ***, $p < 0.001$; for total mitochondrial volume graph (left), CCCP treated HT-1080 cells relative to DMSO treated HT-1080 cells, DMSO treated Gp78 KO clones relative to DMSO-treated HT-1080 cells and CCCP-treated Gp78 KO clones relative to CCCP-treated HT-1080 cells; Mean ± SEM; Scale Bars: 5 μm; 1 μm for zooms)
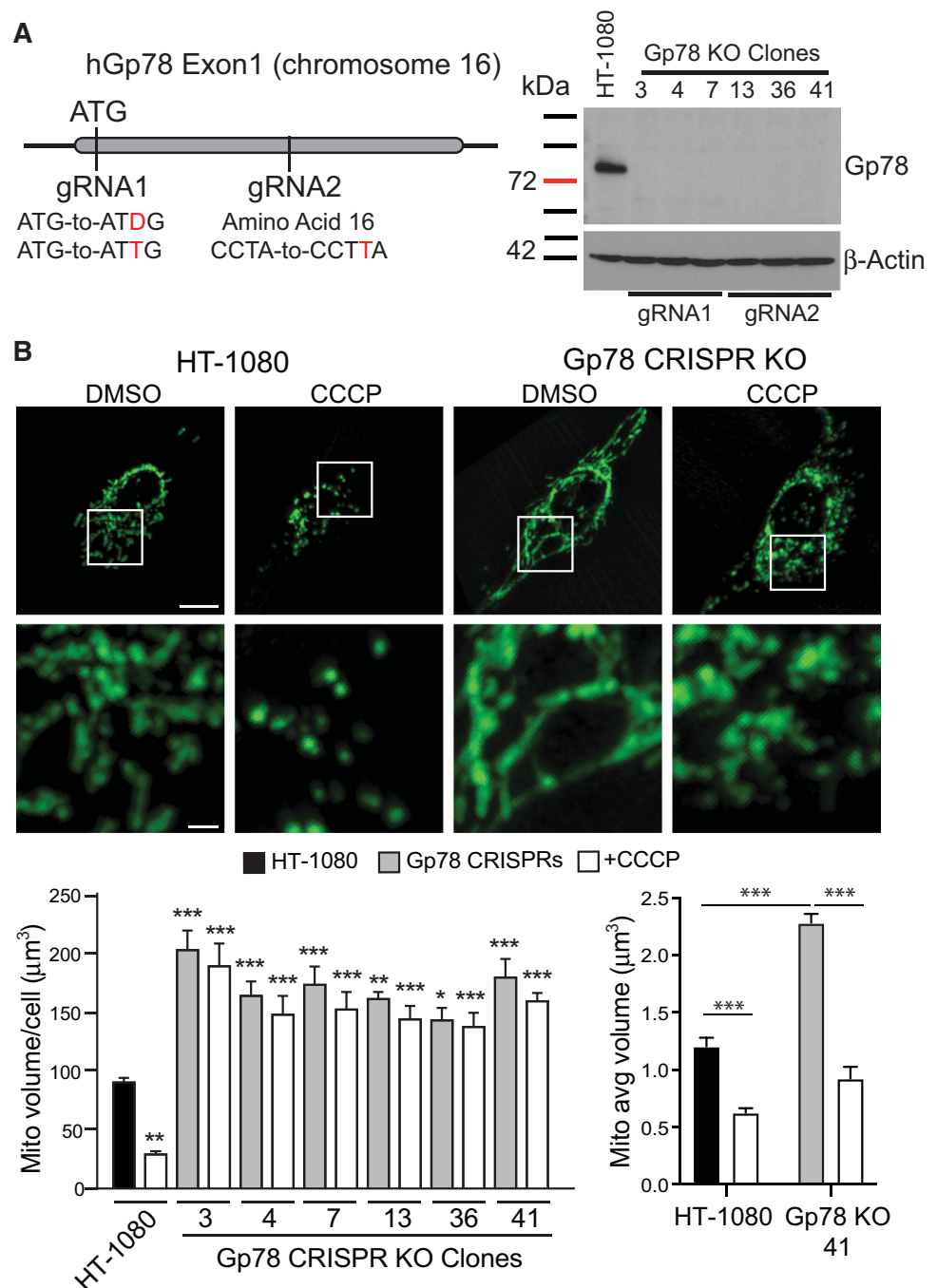
wild-type HT-1080 cells. Quantification of total mitochondrial volume from 3D spinning disk confocal stacks showed a significant ~2-fold increase in total mitochondrial volume per cell as well as average size per mitochondrial segment in the Gp78 knockout clones relative to wild-type HT-1080 cells (Fig. 1B). Rescue of Gp78 knockout HT-1080 cells by transfection of wild-type Gp78, but not Gp78 containing a point mutation in the RING finger domain required for Gp78 ubiquitin ligase activity and mitophagy [34, 38, 46], reduced mitochondrial volume confirming that Gp78

ubiquitin ligase activity controls mitochondrial volume in HT-1080 cells (Supp. Figure 2). To determine if Gp78 knockout specifically affects mitophagy, we assessed the impact of the mitochondrial membrane potential decoupler CCCP on mitochondrial volume in wild-type and Gp78 knockout HT-1080 cells. CCCP treatment induced mitochondrial fragmentation, reflected in a reduced average size of mitochondrial segments in both wild-type and Gp78 KO HT-1080 cells, and a significant reduction in total mitochondrial volume per cell in wild-type HT-1080 cells.

However, while CCCP treatment induced fragmentation of mitochondria of Gp78 knockout HT-1080 cells, the elevated mitochondrial volume of the Gp78 knockout clones was not reduced (Fig. 1B). While varied expression of mitochondrial fusion and fission proteins was observed between Gp78 KO clones (Supp. Figure 1A), increased mitochondrial volume and resistance to CCCP-induced mitophagy was observed consistently for all six Gp78 KO clones (Fig. 1B). This suggests that endogenous Gp78 is required for damage-induced mitophagy in HT-1080 cells.

To determine whether autophagy was responsible for the reduced mitochondria levels of Gp78 knockout cells, we knocked down the essential autophagy gene ATG5 in wild-type HT-1080 cells and Gp78 knockout g1-4 and g2-41 clones. ATG5 knockdown resulted in significantly increased Gp78 levels in HT-1080 cells (Fig. 2A), consistent with a role for autophagy in Gp78 turnover [44]. By Western blot analysis, mitochondrial ATP synthase subunit β levels showed a significant two-fold elevation in both Gp78 knockout clones relative to wild-type HT-1080 cells (Fig. 2B), consistent with the increased mitochondrial volume of these cells (Fig. 1B). Upon ATG5 siRNA knockdown, ATP synthase subunit β levels in HT-1080 cells increased to those of Gp78 knockout cells (Fig. 2B). Similarly, ATG5 KD significantly increased mitochondrial volume by 3D spinning disk confocal analysis of both untreated and CCCP-treated wild-type HT-1080 cells (Fig. 2C). ATG5 KD did not affect mitochondrial volume
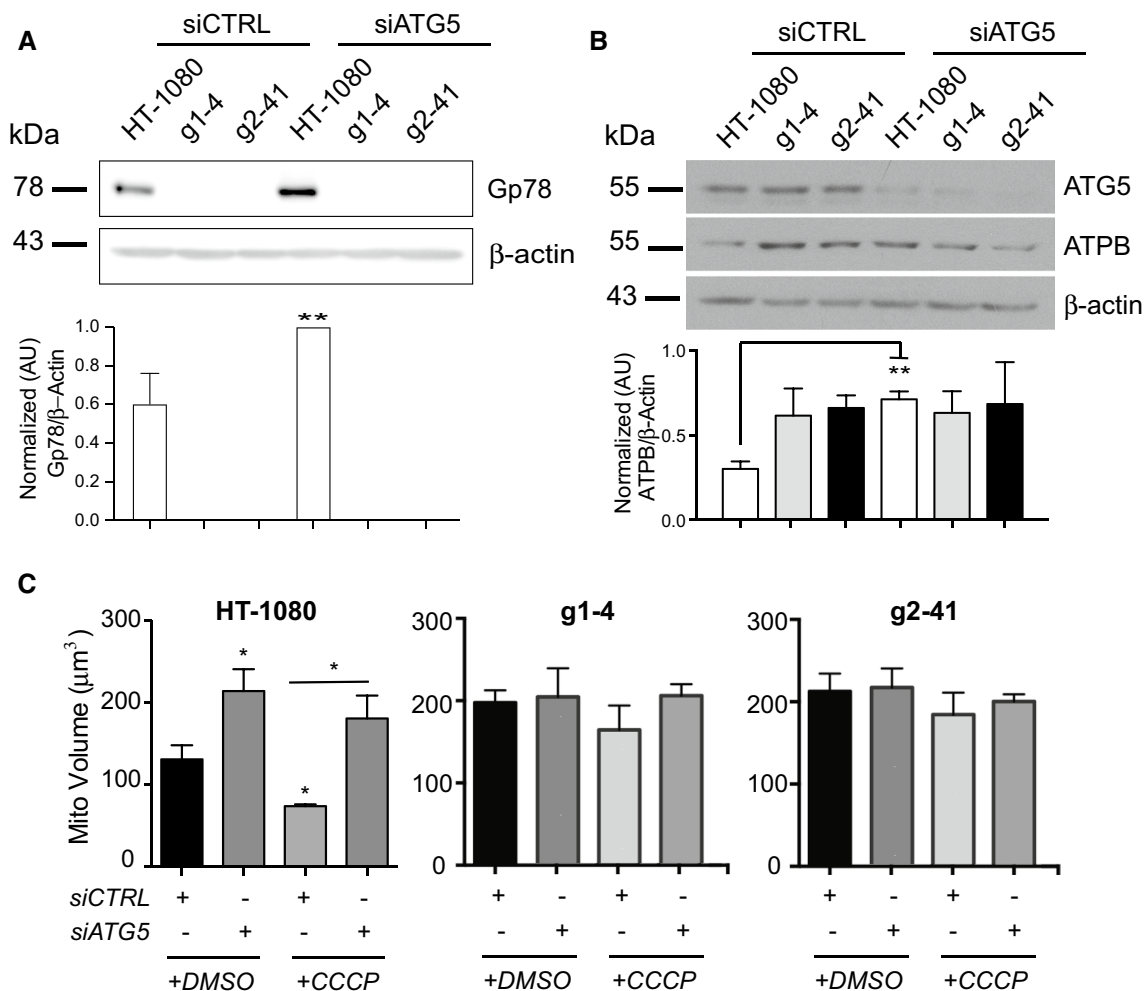

Fig. 2 Gp78 induces basal mitophagy in HT-1080 cells. A Wild-type HT-1080 cells and the g1-4 and g2-41 Gp78 knockout CRISPR clones were transfected with non-specific siCTL or siATG5 and western blotted for Gp78 and β-actin. B Wild-type and Gp78 KO HT-1080 cells, as described in A, were western blotted for ATG5, mitochondrial ATP synthase subunit β (ATPB) and β-actin. Densitometry quantification of Gp78 and ATBP relative to β-actin is shown in the bar graphs (t test; n = 3; **, p < 0.01; Mean ± SEM; full blots shown in Supp. Figure 6). C Wild-type HT-1080 cells and the g1-4 and g2-41 Gp78 knockout CRISPR clones transfected with non-specific siCTL or siATG5 were incubated with either DMSO or 10 μM CCCP for 24 h and then fixed and labeled for mitochondrial ATPB and imaged by 3D spinning disk confocal microscopy. Quantification of total mitochondrial volume is shown in the bar graph. (n = 3 independent biological replicates; > 10 cells/condition per experiment; *, p < 0.05; Mean ± SEM)

in Gp78 knockout clones in the absence or presence of CCCP. This suggests that the increased mitochondrial volume of Gp78 knockout cells, in the absence of CCCP, is due to inhibition of active Gp78-dependent mitophagy in wild-type HT-1080 cells.

We then used the mitoKeima mitophagy probe [50] to test Gp78 regulation of mitophagy in these cells. Excitation maxima of the Keima fluorescent protein is pH sensitive enabling differential detection of mitochondria-targeted Keima in mitochondria, or following mitophagy and delivery to acidic lysosomes. Live cell images of wild-type and Gp78 knockout HT-1080 cells transiently transfected with mitoKeima were ratio analyzed using an ImageJ plugin [51] to detect mitochondrial and lysosomal-associated mitoKeima probe. MitoKeima labeled lysosomes are observed in wild-type HT-1080 cells and to a far lesser extent amongst the extended mitochondrial network of Gp78 knockout cells (Fig. 3). CCCP treatment increased the number and area of mitoKeima-positive lysosomes in wild-type HT-1080 cells indicative of damage-induced mitophagy induction. The Gp78 knockout clone showed no increase in mitoKeima lysosome distribution (Fig. 3). Gp78 knockout in HT-1080 cells is, therefore, associated with impaired basal and damage-induced mitophagy.

Monitoring basal Gp78 mitophagic flux

We then undertook to determine whether Gp78 regulates autophagic flux and more specifically mitophagic flux. We monitored accumulation of the membrane associated LC3B-II by Western blot upon inhibition of lysosomal acidification and degradation using BafA1 (Fig. 4). Cells were treated for 4 h with CCCP to induce mitophagy or serum-starved to induce macroautophagy. With increasing time of BafA1 incubation, cells treated with DMSO or serum-starved showed increased LC3B-II accumulation in both HT-1080 cells and the g1-4 and g2-41 Gp78 knockout clones. Quantification of flux, based on the slope of LC3B-II band density relative to β-actin over time, showed no significant differences between the three cell lines at basal levels. Upon treatment with CCCP, LC3B-II flux was observed in HT-1080 cells but not in the Gp78 knockout clones. These data demonstrate that Gp78 is selectively required for damage-induced mitophagic flux, consistent with the inability of CCCP to induce mitochondrial loss in Gp78 knockout cells (Fig. 1). However, this Western blot analysis did not detect differences in autophagic flux that could explain the increased mitochondrial mass of Gp78 knockout cells, perhaps related to previously reported limitations of
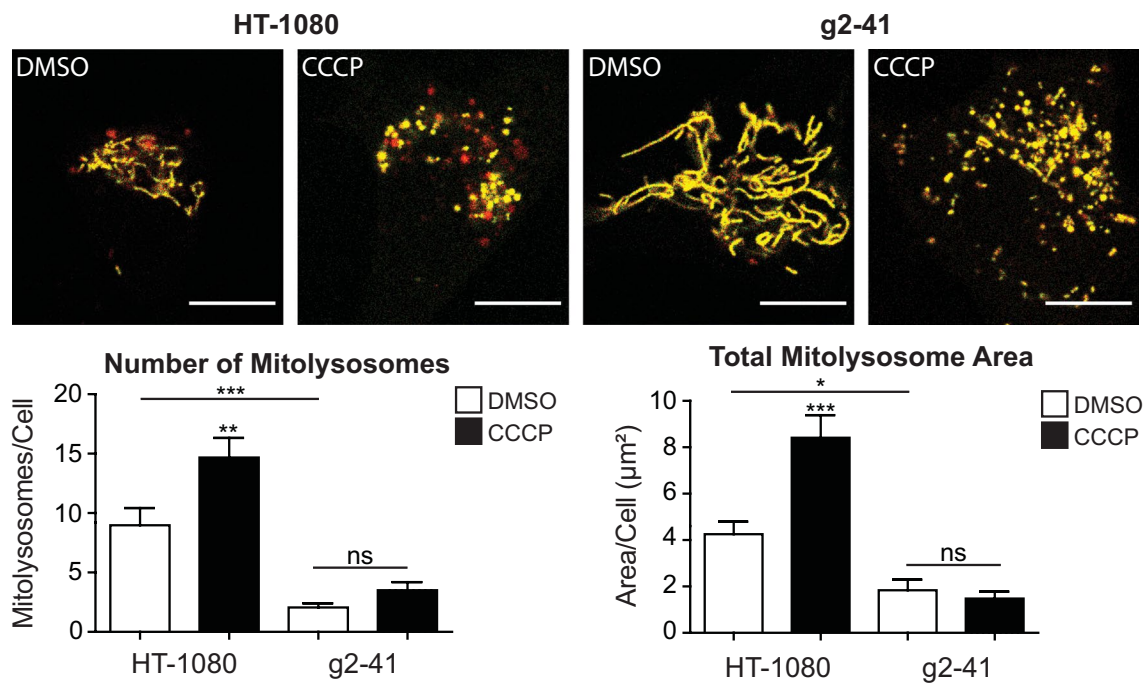

Fig. 3 mitoKeima detection of Gp78-dependent basal mitophagy in HT-1080 cells. Wild-type HT-1080 cells and g2-41 knockout CRISPR clones were transfected with mito-Keima and treated with DMSO or CCCP for 24 h. Confocal fluorescence images show mito-Keima in both neutral (yellow) and low pH (red) environments. Accumulation of mitolysosomes (red) is observed selectively in HT-1080 cells and increased upon CCCP treatment. Quantification of both the number of mitolysosomes per cell and the total area of mitolysosomes per cell is shown in the bar graphs (Scale bar: 10 µm; $n = 3$ independent biological replicates; > 10 cells/condition per experiment; *, $p < 0.05$; **, $p < 0.01$; ***, $p < 0.001$; ns, no significance; Mean ± SEM)
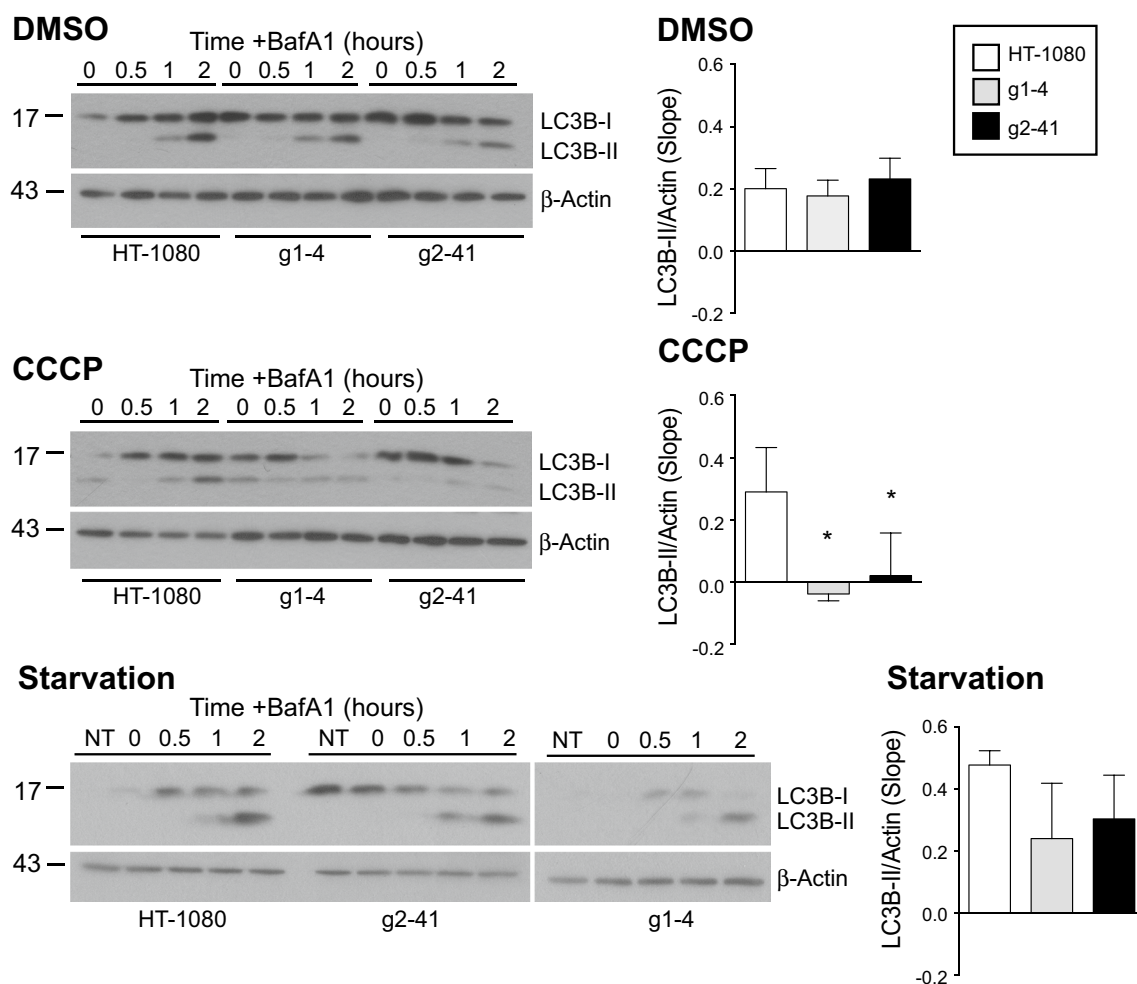
Fig. 4 Flux of autophagy protein LC3B-II in wild-type HT-1080 and Gp78 knockout cell lines. Western blot analysis and probing of LC3B-II in HT-1080 cells and g1-4 and g2-41 Gp78 knockout CRISPR/Cas clones after 4 h treatment with either DMSO, CCCP or starvation in presence of 100 nM of BafA1 for 0, 30, 60 and 120 min. DMSO or serum-starved cells show increased and accumulated LC3B-II with BafA1 in time-dependent manner. The slope of LC3B-II band density quantified relative to β-actin show significant differences between the three cell lines; LC3B-II flux upon CCCP treatment of HT-1080 cells but not in the Gp78 knockout clones can be seen ($n = 4$ independent biological replicates; *, $p < 0.05$; Mean ± SEM; full blots shown in Supp. Figure 7)

Western blot analysis of autophagic proteins for detection of autophagic flux [52, 53].

To develop a more specific and sensitive assay to measure basal autophagic flux, we used the tandem fluorescent-tagged tfLC3 in which LC3 is linked to both GFP and mRFP1; pH-sensitive GFP is a marker for early autophagosomes while mRFP remains fluorescent in acidic autophagolysosomes [54]. Increased dual GFP-mRFP tfLC3 fluorescence upon BafA1 neutralization of acidic autophagolysosomes, enabling GFP fluorescence and preventing GFP degradation is, therefore, an indicator of autophagic flux. Stably expressed tfLC3 in HT-1080 cells presented a diffuse cytosolic distribution in both the GFP and mRFP channels with a few puncta corresponding to autophagic vacuoles (Fig. 5A). Increased accumulation of mRFP puncta relative to GFP puncta, due to mRFP's pH-insensitive fluorescence and

resistance to lysosomal degradation, is indicative of ongoing basal autophagy in these cells [55, 56]. Dually labeled GFP-mRFP puncta correspond to neutral pH autophagosomes; accumulation of dually labeled GFP-mRFP puncta upon short-term BafA1 treatment reflects the accumulation of intact tfLC3 in acidic autophagosomal compartments and is, therefore, a measure of autophagic flux. Upon 4-h CCCP treatment in the presence of BafA1 for the final 2 h, conditions that induce a robust mitophagic flux response (Fig. 4), an increase in both GFP and mRFP labeled puncta was observed, including multiple overlapping puncta (Fig. 5A).

However, quantifying LC3 puncta amongst the diffuse fluorescence signal of cytoplasmic LC3 is challenging [57]. Application of the SPECHT spot detection algorithm was used to robustly identify LC3 puncta [45]. To remove puncta smaller than the 250 nm resolution of diffraction
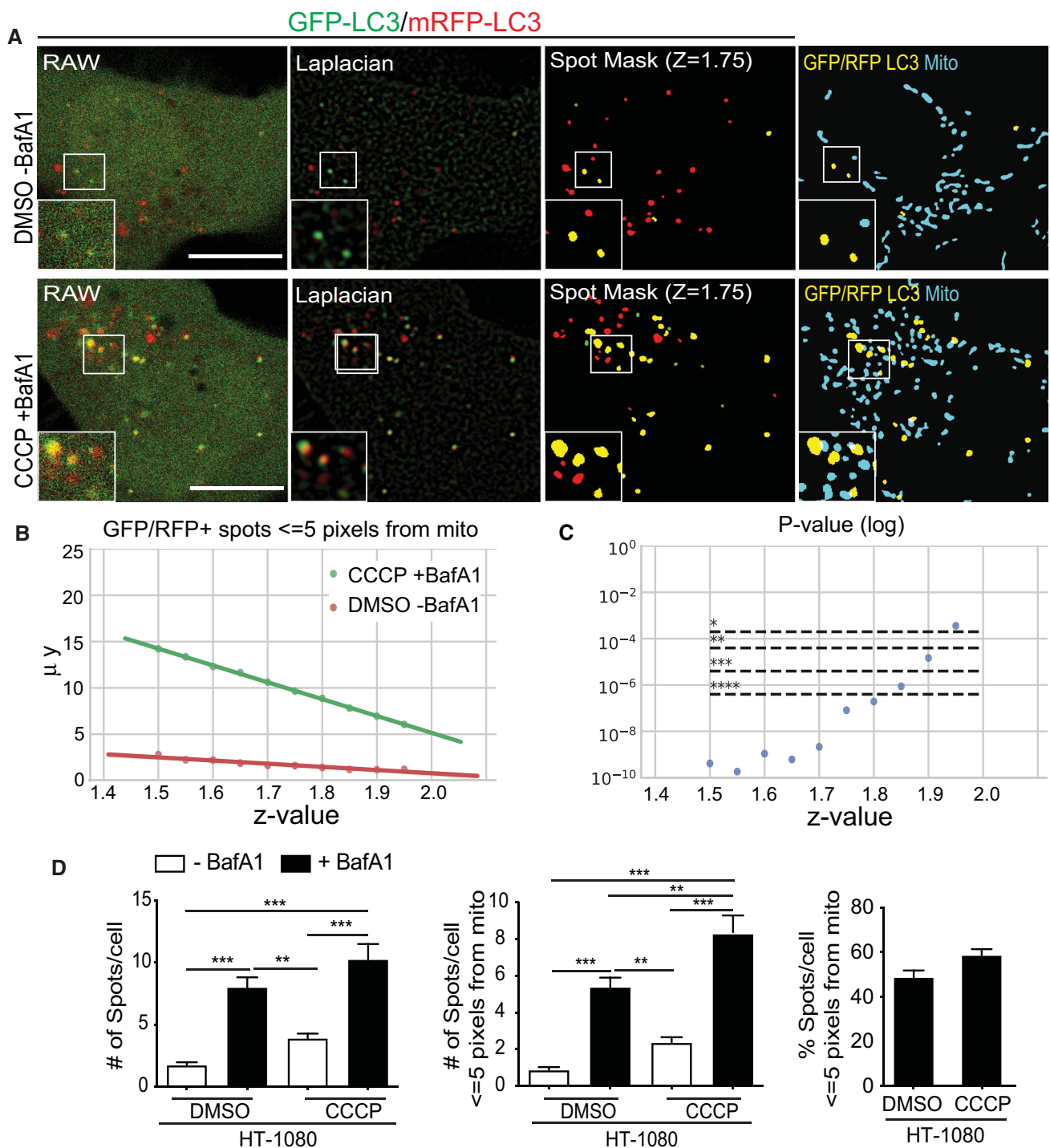
Fig. 5 SPECHT spot detection detects tfLC3 puncta and basal tfLC3 flux. **A** Raw confocal images, Laplacian transforms and SPECHT ($z=1.75$) spot detection of GFP (green) and RFP (red) tfLC3 signal as well as overlay of GFP-RFP-positive tfLC3 puncta (yellow) with a mask of MitoTracker Deep Red FM mitochondrial labeling (blue) are shown. **B** A parameter sensitivity study testing various z-values to determine the significance levels between overlapping GFP-mRFP tfLC3 spots in HT-1080 cells treated with either DMSO or with CCCP and BafA1. Y-axis denotes the mean number of detected spots. **C** A parameter sensitivity study testing various z-values and their effect on the mean of number of overlapping GFP-mRFP tfLC3

spots per cell with mitochondria, within or equal to the 5-pixel unit resolution limit. Bonferroni correction with $m=252$ is applied to correct for multiple hypothesis testing. The Kruskal non-parametric test is applied to test if the samples originate from the same distribution. **D** Bar graphs show the number of overlapping GFP-LC3 and mRFP-LC3 spots per HT-1080 cell treated with DMSO or CCCP $\pm$ BafA1, total and in association with mitochondria, per cell (Mean $\pm$ SEM; $n=6$ independent biological replicates; 10–20 cells/ condition per experiment; *, $p<0.05$; **, $p<0.01$; ***, $p<0.001$; ****, $p<0.0001$). Scale bar, 10 μm

limited confocal microscopy that could not correspond to 300–1000 nm autophagosome precursors or phagophores [58], we applied a size filter that removed any puncta of 25 pixel area (pixel size = 56.6 nm) or less. Overlapping GFP and mRFP puncta (by at least one pixel), considered to be dually labeled GFP-mRFP puncta (spots), are highlighted in yellow and shown overlaid with the mask of the mitochondrial signal (Fig. 5A).

To identify the intensity-independent z score threshold (see Materials and Methods–spot detection) value that most accurately detects LC3-positive autophagosomes, we performed a parameter sensitivity study on z. We tested the impact of z on differential association of autophagosomes with mitochondria between DMSO and CCCP + BafA1-treated cells, known to present a highly significant difference in autophagic flux (Fig. 4). A total of 21 z-values were tested, with values of $z > 2$ resulting in empty image masks. Given that we have 4 groups (CCCP ± BafA, DMSO ± BafA), we have 6 possible combinations (from 4 choose 2) and 2 cell lines ($m = 6 \times 2 \times 21 = 252$ hypothesis tests). To account for multiple testing correction, we applied the Bonferroni correction with a corrected α of $\alpha/252$ and the Kruskal nonparametric test to compare if the difference between the 2 conditions is significant and consistent across the parameter range. Low z values causes higher recall of objects, which possibly skews the results towards significance. At the other end, high z values erode the size and diminishes the counts of detected puncta (Fig. 5B, Supp. Figure 3). Application of SPECHT to size filtered LC3 at $z = 1.75$ dramatically improved LC3 puncta detection, significantly detecting differential expression of dually labeled GFP-mRFP tfLC3 puncta between control and CCCP + BafA1 treated cells and accurately reproducing puncta distribution (Fig. 5C, Supp. Figure 3). Two hours BafA1 treatment induced dually labeled GFP-mRFP tfLC3 puncta not only in CCCP-treated cells but also in untreated cells, indicative of active basal autophagy in HT-1080 cells. BafA1-induced GFP-mRFP tfLC3 puncta encompass both neutral autophagosomes and acidic autophagolysosomes, that following the sequestration event will move away from mitochondria. About 50% of BafA1-induced GFP-mRFP tfLC3 puncta were located within the resolution limit of 5 pixels (~250 nm) to mitochondria for both untreated and CCCP-treated cells (Fig. 5D), indicative of a similar mitochondria association of autophagic vacuoles under basal and CCCP conditions. SPECHT analysis of tfLC3, therefore, detects both basal and damage-induced mitophagic flux in HT-1080 cells.

Having established conditions to detect mitochondria-associated autophagosomes in HT-1080 cells in response to CCCP, known to induce mitophagy in HT-1080 cells, we then applied this approach to HT-1080 and Gp78 knockout g2-41 cell lines in the absence of CCCP. Time course analysis of tfLC3 expression showed a significant increase in dual labeled GFP-mRFP LC3 spots upon 4 h BafA1 treatment of HT-1080 cells in proximity to mitochondria (Fig. 6A). Dual labeled GFP-mRFP LC3 spots showed no increase in the absence of BafA1 or in g2-41 Gp78 knockout cells in the presence of BafA1. The BafA1-induced increase in GFP-mRFP-positive tfLC3 spots in the absence of CCCP is indicative of basal autophagic flux and association of tfLC3 puncta to mitochondria suggestive of basal mitophagy. Inhibition of autophagy by siRNA knockdown of the essential autophagy gene ATG5 (siATG5) prevented BafA1 induction of GFP-mRFP-positive tfLC3 puncta, confirming that this assay reports on basal autophagic processes (Fig. 6B). The close proximity of the majority of GFP-mRFP-positive tfLC3 puncta to mitochondria in HT-1080 cells indicates that SPECHT analysis tfLC3 is reporting on Gp78-dependent basal mitophagy.

Gp78 mitophagy promotes mitochondrial health and limits ROS production

We then tested whether Gp78-dependent basal mitophagy impacts mitochondrial potential, and mitochondrial ROS. HT-1080 and g2-41 Gp78 knockout cells were incubated with MitoView 633, a potential-dependent mitochondrial reporter, or MitoSOX Red, a mitochondrial ROS reporter and imaged by live cell microscopy. MitoView 633 labeling of HT-1080 cells was significantly reduced by both Gp78 knockout and ATG5 siRNA knockdown (Fig. 7A). Mitochondrial potential in Gp78 KO cells approached but remained significantly higher than levels detected upon treatment of cells with CCCP (Supp. Figure 4A). Reduced mitochondrial potential of Gp78 KO HT-1080 cells was Gp78 ubiquitin ligase-dependent and not a result of deficient mitophagy due to mitochondrial hyperfusion (Fig. 1B) as only expression of wild-type Gp78, but not Ring finger mutant Gp78 or the mitochondrial fission protein DRP-1, was able to restore mitochondrial potential in these cells (Supp Fig. 4B). In contrast, Gp78 knockout and ATG5 siRNA significantly increased MitoSOX Red labeling of mitochondrial ROS (Fig. 7B). The parallel effect of both Gp78 knockout and ATG5 knockdown indicates that basal mitophagy promotes mitochondrial health and limits ROS production in HT-1080 cells. That siATG5 did not affect either MitoView 633 or MitoSOX labeling in Gp78 knockout HT-1080 cells suggests that Gp78 is the key regulator of autophagic mitochondrial quality control in these cancer cells.

To test whether Gp78 regulated mitochondria potential in cell lines other than HT-1080, we identified three cancer cell lines, HeLa, PC3 prostate cancer cells and PANC-1 pancreatic cancer cells, exhibiting elevated Gp78 by DepMap analysis (https://depmap.org/portal/). As seen in Fig. 7C, these three cell lines showed reduced Gp78 levels compared
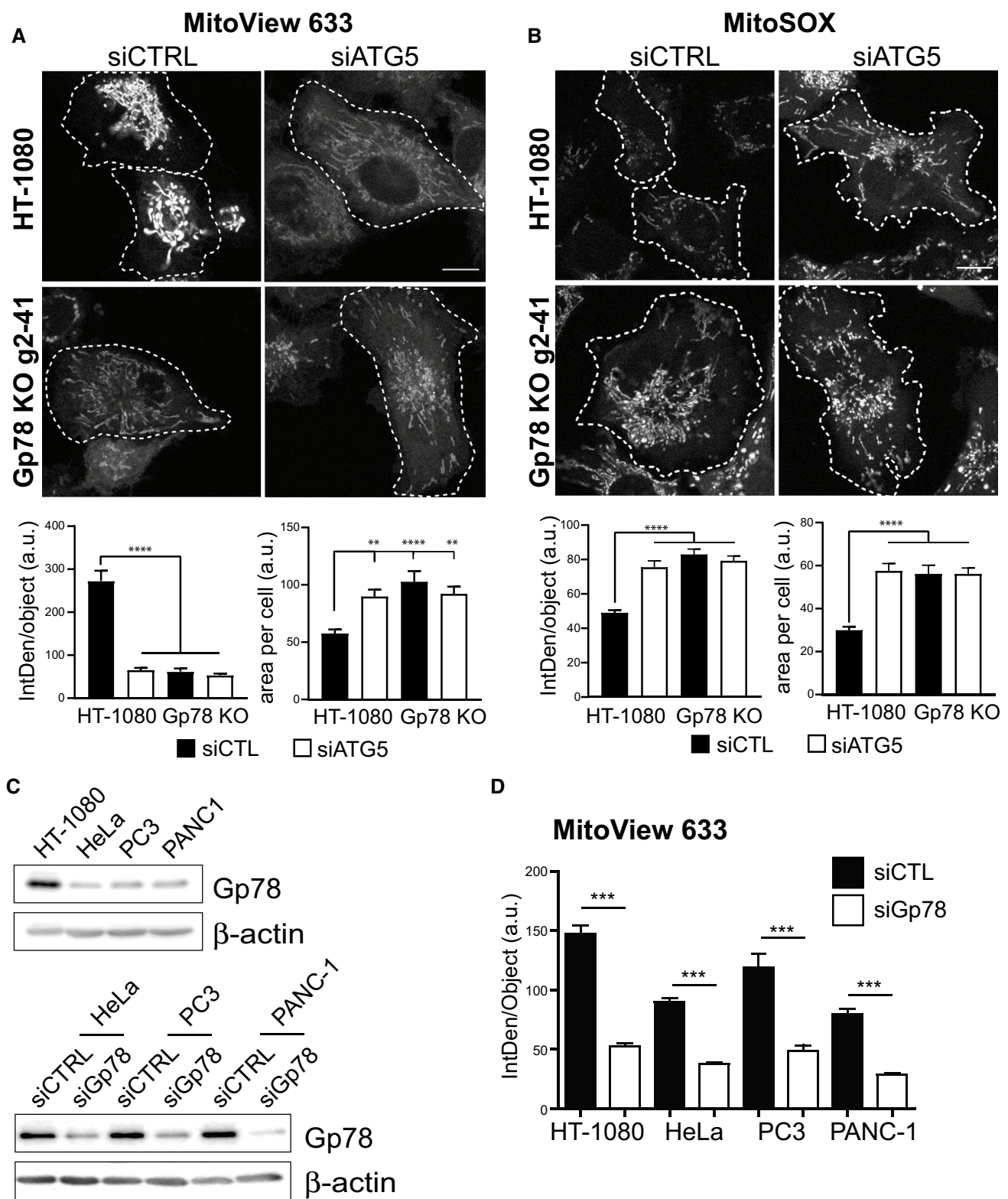
Fig. 6 Gp78 knockout in HT-1080 cells results in impaired tfLC3 flux. **A** Masks of GFP-mRFP-positive tfLC3 puncta (yellow) and mitochondria (blue) in live HT-1080 and g2-41 cells stably transfected with tfLC3 and labelled with the mitochondrial dye MitoTracker Deep Red FM. Live cells were either treated with 100 nM BafA1 and imaged at the indicated time points. Bar graphs show the number of GFP-mRFP-positive tfLC3 puncta, total and in association with mitochondria, per cell (Mean ± SEM; $n = 3$ independent biological replicates; > 10 cells/condition per experiment; *$p < 0.05$; **$p < 0.01$). Scale bar, 10 μm. **B** GFP-mRFP-positive tfLC3 puncta (yellow) and mitochondria (blue) masks of HT-1080 and g2-41 Gp78 knockout cells stably transfected with tfLC3 and labelled with mitochondrial dye MitoTracker Deep Red FM transfected with either control of siATG5 siRNA and treated with 100 nM BafA1. Bar graphs show the number of GFP-mRFP-positive tfLC3 puncta, total and in association with mitochondria, per cell (Mean ± SEM; $n = 3$ independent biological replicates; 10–20 cells/condition per experiment; *$p < 0.05$; ***$p < 0.001$; ns, no significance). Scale bar, 10 μm
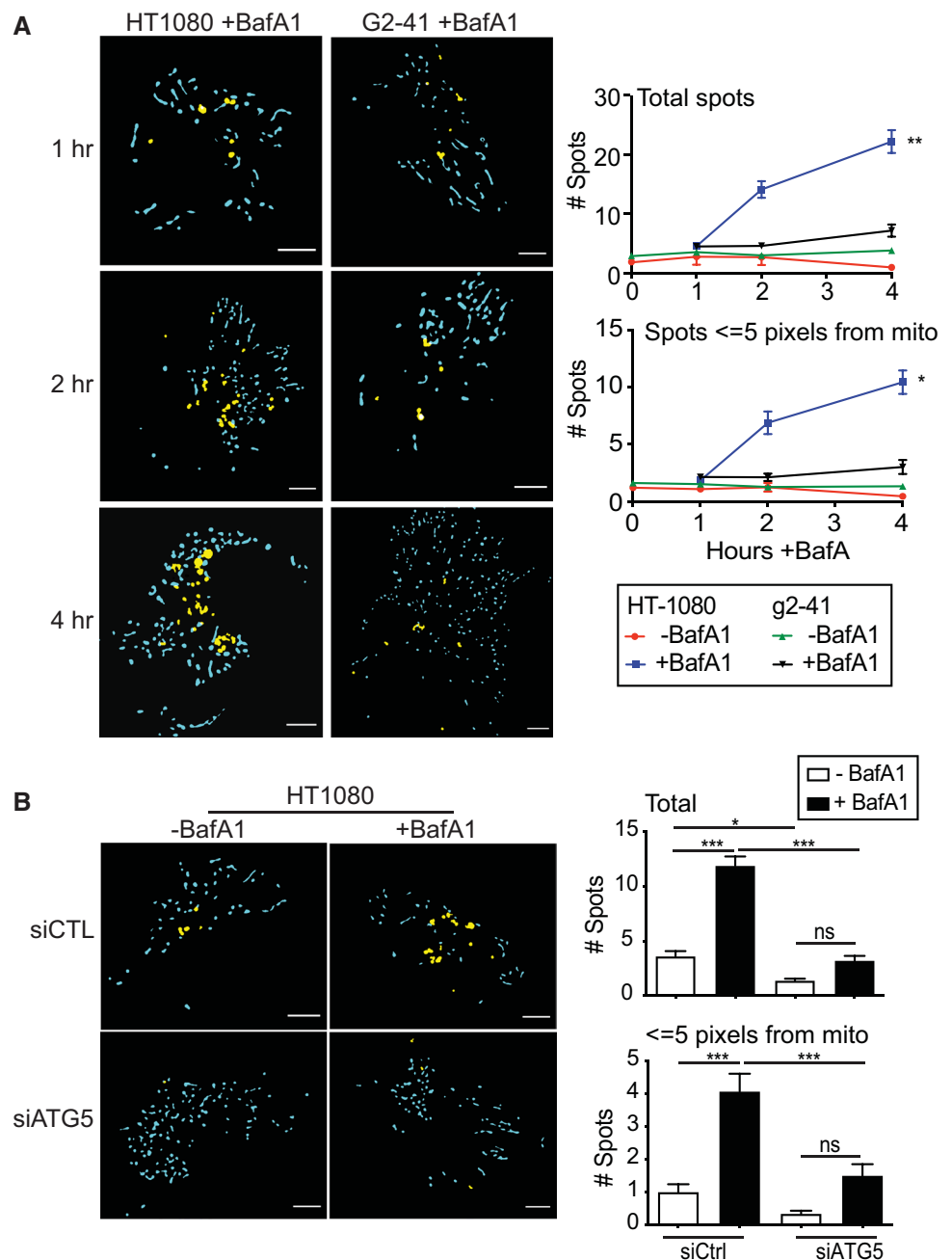
to HT-1080 cells, highlighting the utility of HT-1080 cells as a cell model for Gp78 functional analysis. siRNA knockdown of Gp78 significantly reduced mitochondrial potential in all four cell lines (Fig. 7C, D), supporting a general role for Gp78 in the regulation of the mitochondrial health of cancer cells.

Live cell time lapse imaging of tfLC3-expressing HT-1080 cells labeled for MitoView 633 was performed to determine if autophagosomes specifically associate with damaged mitochondria, i.e. those showing reduced mitochondrial potential. Cells presenting multiple GFP LC3 puncta were imaged by spinning disk confocal and image

stacks, seven images at 500 nm spacing to cover the depth of the cell and minimize overlap of autophagosomes in different Z-sections, were acquired every minute over 40 min. SPECHT analysis identified dual-labeled GFP-mRFP tfLC3 puncta, corresponding to phagophores or autophagosomes, in every frame. Representative time lapse images are presented in Fig. 8A. Dual-labeled GFP-mRFP tfLC3 puncta were observed to associate with MitoView 633 labeled mitochondria. To determine if autophagosomes were more closely associated with lower potential mitochondria, we quantified the average intensity of MitoView 633 positive pixels overlapping GFP-RFP-positive tfLC3 puncta relative

MitoView 633

A

	siCTRL	siATG5

HT-1080

Gp78 KO g2-41

B

MitoSOX

	siCTRL	siATG5

HT-1080

Gp78 KO g2-41

C

D

MitoView 633

to average MitoView 633 intensity in either the complete mitochondrial segment overlapping the autophagosome or in the whole cell. MitoView-positive pixels overlapping GFP-mRFP-positive tfLC3 puncta presented a below average

mitochondrial potential. Time lapse series acquired every 10 s show the dynamic association of GFP-mRFP-positive tfLC3 puncta with low potential mitochondria (Fig. 8B; Supp. Video 1). These data show that autophagosomes

◄**Fig. 7** Basal mitophagy maintains healthy mitochondria and limits ROS production. HT-1080 and Gp78 knockout g2-41 HT-1080 cells were transfected with siCTL (black bars) or siATG5 (white bars) and labeled with either the mitochondrial potential reporter MitoView 633 **A** or the mitochondrial ROS probe MitoSOX **B** for 30 min. Live confocal images are shown and integrated density of MitoView 633 and MitoSOX per mitochondrial object and mitochondrial area per cell were quantified. **C** Western blot analysis of Gp78 an β-actin in HT-1080, HeLa, PC3 and PANC-1 cells and for the latter three following siRNA knockdown of Gp78 (Full blots shown in Supp. Figure 8). **D** HT-1080, HeLa, PC3 and PANC-1 cells were transfected with siCTL (black bars) or siGp78 (white bars) and labeled with MitoView 633. Integrated density of MitoView 633 per mitochondrial object was quantified. ($n = 3$ independent biological replicates; > 15 cells/condition per experiment; **, $p < 0.01$; ***, $p < 0.001$, ****, $p < 0.0001$). Scale Bar, 10 μm

in HT-1080 cells associate with damaged mitochondria, thereby contributing to maintenance of mitochondrial health of these cells.

Tumor expression of Gp78

To determine the effect of deficient mitophagy on tumor growth, we generated sub-cutaneous xenograft tumors for wild-type HT-1080 cells and the six Gp78 KO clones. As previously reported for Gp78 shRNA knockdown [41], we observed no significant effects of Gp78 KO on HT-1080 tumor growth (Supp. Figure 4C). However, consistent with our in vitro findings, labeling of tumor sections showed significantly elevated mitochondrial labeling for all six Gp78 KO clones (Fig. 9A). Furthermore, labeling of tumor sections showed significantly elevated expression of the Ki67 cell proliferation reporter in three of the Gp78 KO clones and reduced labeling of the TUNEL cell death marker in a majority of the six Gp78 KO clones relative to wild-type HT-1080 cells (Fig. 9A). These xenograft tumor data support a role for Gp78-dependent mitophagy in the suppression of cancer cell proliferation.

To assess the expression of Gp78 in multiple cancers, we used GEPIA-2 analysis to probe TCGA RNAseq data for mRNA expression of Gp78 and other ubiquitin ligases that induce mitophagy (PARK2, RNF185, MUL1, MARCH5, HUWE1, SIAH1) as well as the hypoxia-induced mitophagy proteins BNIP and NIX [59]. Figure 9B highlights the overall generally elevated expression of Gp78 relative to the majority of these mitophagy regulating proteins, and certainly of PARK2, in the vast majority of cancers studied. Gp78 also exhibits a distinct cancer specific expression profile relative to other cancer-associated mitophagy inducers such as HUWE1, BNIP and NIX. Importantly, Gp78 expression can be both significantly upregulated and downregulated in different cancers or show no significant change, such as in sarcoma or breast cancer (Fig. 9C). Therefore, while Gp78 is generally expressed in a multitude of cancers,

its role as a tumor suppressor via regulation of mitophagy may be cancer-type specific.

Discussion

Here, using CRISPR/Cas9 knockout in the HT-1080 fibrosarcoma cell line, we show that the Gp78 ubiquitin ligase controls basal mitophagic flux and thereby mitochondrial health and ROS production. Basal autophagy maintains cellular homeostasis through the sequestration and subsequent removal of bulk cytoplasmic constituents by delivery to lysosomes for degradation. Basal autophagy has been shown to selectively target subcellular components such as lipids and organelles [60–63]. Functional consequences of defective basal autophagy in ATG5 knockout mice include thyrocyte death, neurodegeneration and increased oxidative stress associated with elevated ROS in these cell populations, possibly because of the accumulation of damaged mitochondria [64, 65]. The deficient mitochondrial metabolic activity and increased ROS production associated with the impaired basal mitophagy of Gp78 knockout HT-1080 cells provides a definitive link between basal mitophagy, maintenance of mitochondrial health and ROS production by cancer cells.

Detecting basal mitophagy

As a dynamic, multistep process, autophagic activity is best measured by transit through the path, or autophagic flux [66]; however, measuring basal autophagy, or autophagic flux in the absence of autophagy inducers, is challenging. Mitophagy is monitored through loss of mitochondrial mass; increased mitochondrial volume upon Gp78 knockout and increased mitochondrial mass upon ATG5 siRNA knockdown was indicative of increased basal mitophagy in HT-1080 cells. Reporters like mito-Keima and Mito-Qc report on delivery of mitochondrial proteins to lysosomes and have proven invaluable to monitor mitophagic flux to lysosomes in cells and tissues [23, 50, 67, 68]. Use of mitoKeima and ratio imaging analysis was able to detect the elevated damage-induced and basal mitophagy in wild-type HT-1080 relative to Gp78 knockout cells. However, these approaches report on late stages, i.e. lysosomal delivery and degradation, of mitophagy.

Approaches to measure earlier stages of autophagic flux include analysis of phagophore- and autophagosome-associated LC3B-II and targeted knockdown or knockout of essential autophagy proteins [57]. Western blotting of expression levels of autophagy proteins, such as LC3B-II, report on autophagic activity in a cell population but are limited in their ability to directly measure flux [53]. Western blotting of LC3-II in BafA1 treated cells detected autophagic flux in response to serum starvation and, selectively for wild-type
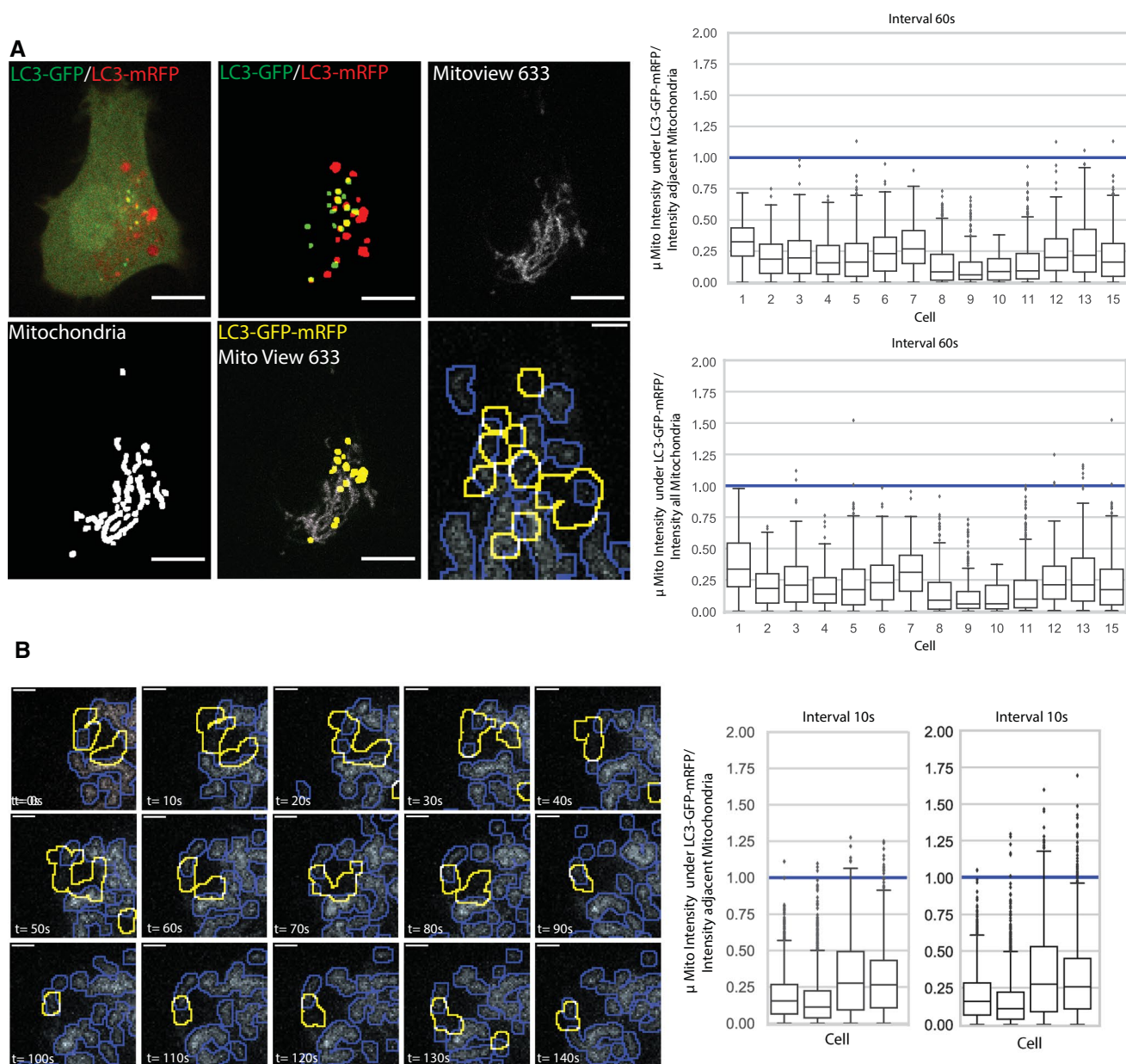
Fig. 8 Time lapse imaging of tfLC3 in HT-1080 cells shows autophagosome association with low potential mitochondria. **A** Z-stacks (7 images; 500 nm spacing; $n = 3$ independent biological replicates; 15 cells) of HT-1080 cells expressing tfLC3 and labeled with MitoView 633 were acquired by spinning disk confocal every minute over 40 min and processed by SPECHT to reveal GFP-mRFP-positive tfLC3 puncta and mitochondria. A representative image of a single Z-section shows SPECHT processing of tfLC3 and mitochondria signals (Scale bar: 10 μm). ROI shows overlap of autophagosomes with lower potential mitochondria (Scale bar: 2 μm). Average intensity of MitoView 633 positive pixels overlapping GFP-mRFP-positive tfLC3 puncta was quantified relative to the average of all MitoView 633 positive pixels in the adjacent mitochondrial segment or in all mitochondrial segments in the cell. For each GFP-mRFP-positive tfLC3 puncta in any of the 7 Z-slices, the ratio of overlapping mitochondria pixels relative to adjacent mitochondria segment and all mitochondria segments in the cell is shown per cell as a boxplot (< 1: fainter than average; > 1 brighter than average). **B** Image series from time lapse movies, as described in (**A**), acquired every 10 s are shown (see Supplemental Video 1). Boxplots are as described in (**A**). (Scale Bar, 2 μm; $n = 4$)

but not Gp78 knockout cells, upon CCCP treatment. This supports a selective deficiency in mitophagy and not general autophagy upon Gp78 knockout. However, Western blotting for LC3B-II was not sensitive enough to detect differences in basal autophagic flux between cell types.

Fluorescent LC3 expression reporters such as GFP-LC3 and tfLC3 have been used to study autophagic flux in

cells and tissues [23, 50, 67, 68]. Tandem tfLC3 reports on autophagic flux at the level of autophagosome maturation due to the differential sensitivity of GFP and mRFP to acid quenching of fluorescence and degradation in lysosomes. However, analysis and interpretation of the acquired data remain challenging. Segmenting LC3 puncta from cytoplasmic LC3 fluorescence is difficult, such that, in some cases, manual counting of LC3 puncta is required [57, 69]. By applying the spot detection stage of the SPECHT algorithm [45], we report the sensitive and robust detection of tfLC3 puncta. BafA1 inhibition of autophagosome maturation using tfLC3 demonstrates the presence of basal autophagic flux in HT-1080 cells but not in Gp78 knockout HT-1080 cells. Mapping of mitophagy and macroautophagy in the eye shows that the extent to which mitophagy contributes to macroautophagy is cell type specific [70]. The reduced tfLC3 autophagic flux upon Gp78 KO, together with the close mitochondrial association of autophagosomes, the reduced mitochondria potential and increased mitochondrial ROS upon siATG5 inhibition of autophagy, suggests that Gp78-dependent mitophagy is a major component of basal autophagic flux in HT-1080 cells. Live cell time lapse analysis of tfLC3 in HT-1080 cells allowed us to demonstrate that autophagosomes associate with reduced potential mitochondria, confirming a role for mitophagy in mitochondrial quality control. The enhanced sensitivity of detection of tandem tfLC3 using SPECHT [45], even when channels differ markedly in signal to noise ratio, renders this a valuable tool to study basal autophagy in various cell and tissue systems.

Gp78, mitophagy and ROS production

Gp78 overexpression recruits LC3 to mitochondria-associated ER [34] and Gp78 has been shown to selectively regulate rough ER-mitochondria contacts [47]. Also, Gp78 has been recently shown to be involved in ER-phagy, and selective degradation of the outer mitochondrial membrane, forming mitoplasts and triggering mitophagy [44]. The increased levels of Gp78 reported here upon ATG5 knockdown in HT-1080 supports autophagic degradation of Gp78 (i.e. ER-phagy); however, the relationship between Gp78-dependent mitoplast formation, the ER and the dynamic movement and maturation of LC3-positive autophagosomes in proximity to mitochondria that we report here remains to be determined. Considering the dispensable role of Parkin and PINK1 in basal mitophagy in vivo [23, 29], further analysis of the role of Gp78-dependent basal mitophagy in tissue development and cancer progression is warranted. The reduced mitochondrial potential of HeLa, PC3 and PANC1 cells upon Gp78 siRNA knockdown supports a general role for Gp78 mitophagy in the regulation of mitochondrial health of cancer cells. Indeed, GEPIA-2 analysis shows the elevated expression of Gp78 across a broad range of tumor types relative to other mitophagy inducing proteins, and in particular Parkin, supports a key role for Gp78 in cancer progression.

ROS generation shows a complex association with tumor progression. ROS are critical for tumor initiation and progression acting through activation of oncogenic signaling and DNA mutation; at the same time, increasing ROS production eliminates cancer cells by inducing cell death programs [71]. Regulation of mitochondrial ROS production by BNIP3, a hypoxia-induced mitophagy regulator, suppresses breast cancer progression [72, 73]. The formation of spontaneous liver tumors after 12 months in Gp78 knockout mice supports a tumor suppressor function for Gp78 [40]. Consistently, we show that increased mitochondrial mass in Gp78 KO HT-1800 xenograft tumors is associated with increased tumor cell proliferation and reduced cell death. These data suggest that Gp78-dependent mitophagic control of ROS production may play a critical role in Gp78 tumor suppressor function.

Previously, Gp78 knockdown in the HT-1080 cells studied here did not affect tumor growth but did inhibit metastasis [41]; further, impaired metastasis was rescued by wild-type Gp78 but not a RING finger Gp78 mutant with deficient ubiquitin ligase activity that does not induce mitophagy [34, 41]. Indeed, Gp78 was shown to promote metastasis though targeted degradation of the metastasis suppressor KAI1 [41] and Gp78 downregulation of KAI1 was associated with mammary gland hyperplasia [74]. Furthermore, Gp78 was recently identified as a poor prognosticator for African-American women with breast cancer [75]. Of interest, analysis of TCGA data shows that Gp78 can show both significantly elevated and reduced global expression in different cancer types as well as no significant changes in global Gp78 expression in multiple tumors, including breast cancer or sarcoma, the cancer of origin for the HT-1080 cell line. This suggests multiple roles for Gp78 in cancer progression, including but not limited to regulation of ROS production through mitophagy, impacted by tumor type as well as other factors extending to tumor subtype and patient ethnicity. Identification of molecular regulators of Gp78 mitophagy function may be key to understanding and targeting Gp78 function in cancer.

Materials and methods

Antibodies and reagents

Anti-ATPB (ATP synthase subunit β) pAb/mAb (ab128743/ab5432), anti-p62 (ab56416), anti-MFN1 (ab57602), anti-MFN2 (ab56889), anti-PINK1 (ab23707), anti-mitochondria [113-1] mAb (ab92824) and anti-DRP1 (ab184247), were purchased from Abcam (Cambridge, MA, USA), anti-ATG5
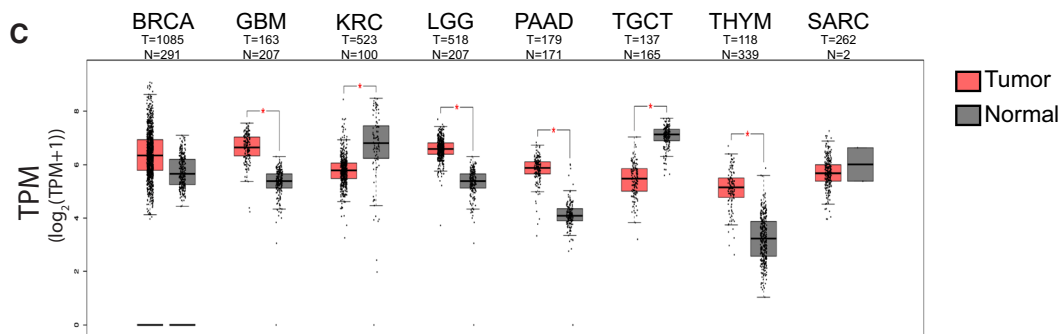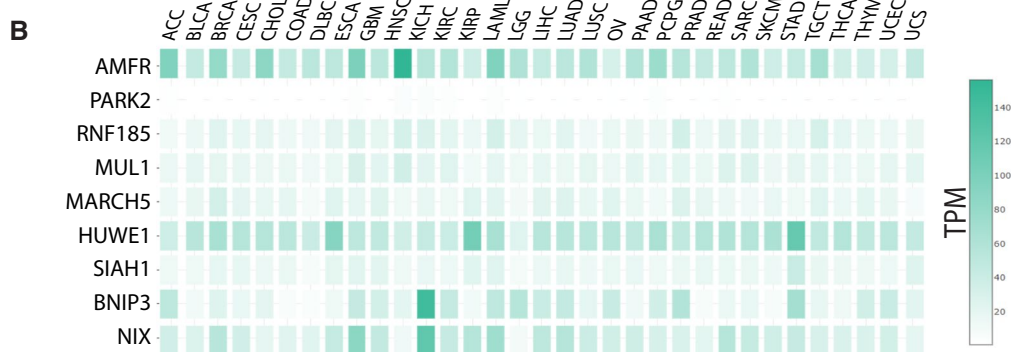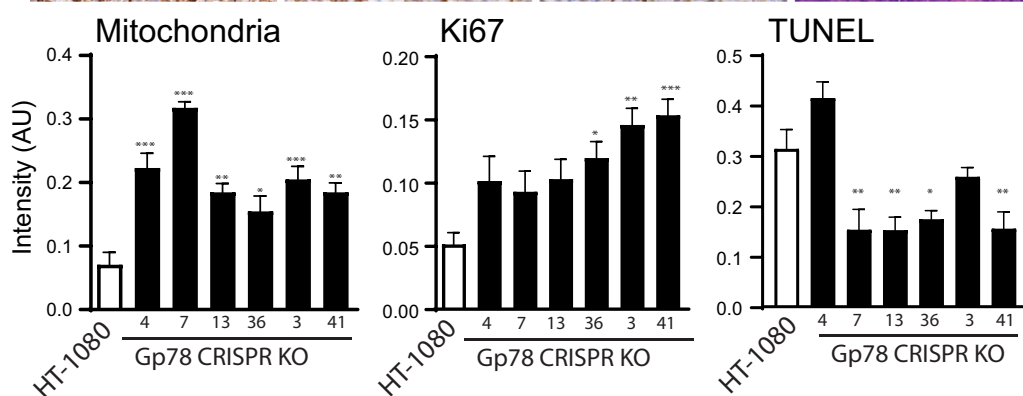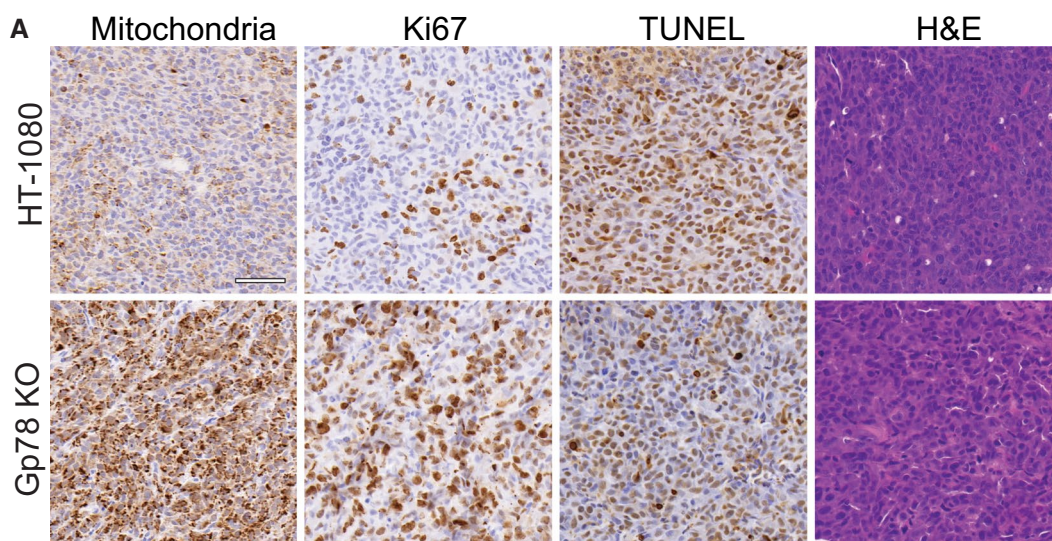
◄**Fig. 9** Gp78 tumor expression. **A** Representative tumor sections stained for mitochondria, Ki67, TUNEL and Hematoxylin and Eosin (H&E) from xenograft s.c. tumors of wild-type HT-1080 cells and a representative Gp78 KO HT-1080 clone. Bar graphs show quantification of labeling for wild-type HT-1080 cells and all 6 Gp78 KO clones (Mean ± SEM; Scale Bar: 20 μm; $n = 5$–6 tissue sections per cell line; *, $p < 0.05$; **, $p < 0.01$; ***, $p < 0.001$). **B** Heatmap of mitophagy regulators (Gp78 (AMFR), PARK2, RNF185, MUL1, MARCH5, HUWE1, SIAH1, BNIP3, NIX) in various cancer types. Gene expression is displayed as transcripts per million (TPM). **C** Boxplots of AMFR (Gp78) gene expression in tumor relative to normal, non-tumoral tissue of same tissue origin. Gene expression is log-scaled ($log_2(TPM + 1)$) and given in transcripts per million (TPM) (*, $p < 0.01$). *ACC* adrenocortical carcinoma; *BLCA* bladder urothelial carcinoma; *BRCA* breast invasive carcinoma; *CESC* cervical squamous cell carcinoma and endocervical adenocarcinoma; *CHOL* cholangio carcinoma; *COAD* colon adenocarcinoma; *DLBC* lymphoid neoplasm diffuse large B-cell lymphoma; *ESCA* esophageal carcinoma; *GBM* glioblastoma multiforme; *HNSC* head and neck squamous cell carcinoma; KICH kidney chromophobe; KIRC kidney renal papillary cell carcinoma; *KIRP* Kidney renal papillary cell carcinoma; *LAML* acute myeloid leukemia; *LGG* brain lower grade glioma; *LIHC* liver hepatocellular carcinoma; *LUAD* Lung adenocarcinoma; *LUSC* lung squamous cell carcinoma; *MESO* mesothelioma; *OV* ovarian serous cystadenocarcinoma; *PAAD* pancreatic adenocarcinoma; *PCPG* pheochromocytoma and paraganglioma; *PRAD* prostate adenocarcinoma; *READ* rectum adenocarcinoma; *SAARC*: sarcoma; *SKCM* skin cutaneous melanoma; *STAD* stomach adenocarcinoma; *TGCT* testicular germ cell tumor; *THYM* thymoma; *UCEC* uterine corpus endometrial carcinoma; *UCS* uterine Carcinosarcoma; *UVM* uveal melanoma

pAb (NB110-53818) from Novus Biologicals (USA), anti-OPA1 (612606) from BD (USA), anti-Gp78 pAb (16675-1-AP) and anti-ULK1 (20986-1-AP) from Proteintech (USA) and anti-LC3B pAb (2775S) from Cell Signaling. Anti-β-Actin mAb (A5441), tissue culture grade DMSO (D2650), Bafilomycin A1 (Cat# C1988) and CCCP (C2759) were purchased from Sigma-Aldrich (USA). mRFP-GFP tandem fluorescent-tagged LC3 (tfLC3) was a gift from Tamotsu Yoshimori (Addgene plasmid # 21074; www.addgene.org/21074) [54]. mKeima-Red-Mito-7 plasmid was a gift from Michael Davidson (Addgene plasmid #56018; www.addgene.org/56018). mCherry DRP-1 plasmid was a gift from Gia Voeltz (Addgene plasmid #49152 (https://www.addgene.org/49152/). MitoTracker Deep Red FM (M22426), Live Cell Imaging Solution (A14291DJ), Glucose Solution (A2494001), MitoSOX Red (M36008) and MEM Non-Essential Amino Acids Solution (11140050) were purchased from ThermoFisher (USA). MitoView 633 (#70055) was purchased from Biotium (USA).

Cell lines and CRISPR/Cas9 knockout of Gp78

PANC1 cells were originally purchased from ATCC (Dr. Calvin Roskelley, LSI, UBC) and gifted to us. HeLa, PC3 and HT-1080 cell lines were acquired from ATCC, authenticated by Short Tandem Repeat (STR) profiling at the TCAG Genetic Analysis Facility (Hospital for Sick Kids, Toronto, ON, Canada www.tcag.ca/facilities/geneticAnalysis.html) and tested regularly for mycoplasma infection by PCR (ABM, Richmond, BC, Canada). Cells were maintained in DMEM (HeLa, PANC1) or RPMI 1604 (HT-1080, PC3) media supplemented with 10% FBS and 1% L-Glutamine in a 37 °C incubator with 5% CO_2.

GeneArt-CRISPR/Cas9 Nuclease vector with OFP (Orange Fluorescence Protein) kit (A21174) was from Life Technologies (Invitrogen, USA). We used http://crispr.mit.edu to design guided RNAs and http://www.rgenome.net/cas-offinder/ (RGEN tools) to check them for off-target effects and used the following oligonucleotides for guide RNA1 (5′-CAC CGG AGG AAG AGC AGC GGC ATG G-3′, 5′-AAA CCC ATG CCG CTG CTC TTC CTC C-3′) and guide RNA2 (5'-CAC CGG CCC AGC CTC CGC ACC TAC A-3', 5'-AAA CTG TAG GTG CGG AGG CTG GGC C-3′). From isolated genomic DNA for each clone, the DNA fragment flanking Exon1 of Gp78 was PCR amplified, cloned and sequenced. For gRNA1 clones #3 and #4, the G was deleted from the ATG start codon, while for clone #7, an additional T was inserted in the start codon generating ATTG. For all three gRNA2 clones (#13, 36, 41), a T was inserted at amino acid 16 (CCTA to CCTTA) causing a frameshift mutation. The guide RNAs were in vitro annealed, cloned into the GeneArt linear vector according to the supplier's protocol and sequence verified prior to transfection into HT-1080 cells. Sequence verified gRNA1 or gRNA2 containing GeneArt-CRISPR/Cas9 Nuclease vector with OFP were transiently transfected into HT-1080 cells, plated 24 h previously, using Effectene transfection reagent (301,425, Qiagen, USA). After 36 h incubation, cells were harvested and genomic DNA isolated to perform GeneArt Genomic Cleavage Detection assay (A24372, Invitrogen, USA) to check cleavage efficiency. Once cleavage efficiency was confirmed, HT-1080 cells were replated for 36 h, trypsinized, FACS sorted and OFP expressing cells were singly plated in 96 well pates by serial dilution. Single colonies were replicated in 12 well plates; one set was frozen and stored in liqN2 and the other set subjected to lysate preparation, SDS-PAGE and Gp78 Western blot analysis. Arbitrarily chosen representative clones (g1-3, g1-4, g1-7; g2-13, g2-36, g2-41) from both gRNAs were expanded, tested for mycoplasma and stored as multiple freeze-downs. From isolated genomic DNA, an approximate 800 bp fragment flanking Exon1 of Gp78 was PCR amplified using Q5 (Qiagen, USA) the following primer set (Forward: 5′-CTG GAG GCT ACT AGC AAA-3′, Reverse: 5′-ATG TGG CCC AGT ACC T-3′) and TA cloned. At least ten clones were sequenced from each to confirm INDEL.

HT-1080 wild-type and Gp78 CRISPR/Cas9 knockout clones were grown only up to six passages. Cells were passed every 48 h at a density of 200,000 cells per 10 cm

petri dish, rinsed every 24 h with 10 ml of PBS and supplied with 10 ml of fresh complete medium. HT-1080 cells and the g2-41 Gp78 CRISPR/Cas9 knockout clones were stably transfected with mRFP-GFP tandem fluorescent-tagged LC3 (tfLC3) plasmid using Effectene (Cat. #301425, Qiagen, USA) following the manufacturer's protocol. After 24 h incubation, transfected cells were selected against G418 (400 ug/ml) for about 14 days. The resistant cell population was pooled and maintained in 50 µg/ml G418.

siRNA knockdown, plasmid transfection and western blotting

siControl, siATG5 and siGp78 (Cat# D-001810-01-05, Cat# L-004374–00-0005, Cat# L-006522-00-0005, respectively) were purchased from Dharmacon and transiently transfected where indicated using Lipofectamine 2000 (Cat# 11668019, Invitrogen, USA) following the manufacturer's protocol. All siRNA transfection experiments were for 48 h and treatments were performed 24 h post-siRNA transfection. Alternatively, cells were transiently transfected with mammalian protein expressing plasmids using Effectene (Qiagen, Germany) following the manufacturer's protocol. Where indicated, cells were treated with 10 µM of CCCP or a corresponding volume of DMSO as control 24 h prior to fixation or harvesting cells. Western blotting was performed as previously described using Horseradish Peroxidase (HRP)-conjugated secondary antibody followed by addition of ECL (GE Healthcare Bio-Sciences Corp., USA) to reveal chemiluminescence on either on X-ray film [74] or using a ChemiDoc (BioRad). Densitometry quantification was done using ImageJ (https://imagej.nih.gov/ij/docs/faqs.html#cite) software. Full, uncropped Western blots can be viewed in Supplemental Figs. 5, 6, 7 and 8.

Fluorescent labeling of mitochondria

For immunofluorescent labeling, cells were: 1) fixed with 3.0% PFA for 15 min at room temperature and washed with PBS-CM (phosphate buffer solution supplemented with 1 mM CaCl2 and 10 mM MgCl2); 2) permeabilized with 0.2% Triton X-100 for 5 min and washed with PBS-CM; 3) blocked with 1% BSA for 1 h at room temperature; 4) labeled with anti-ATPB for 1 h followed by washing with PBS-CM; 5) incubated with secondary antibodies for 1 h followed by washing with PBS-CM; and 6) mounted in ProLong Diamond (ThermoFisher) and cured for 24 h at room temperature before imaging. Confocal image stacks were obtained on a III-Zeiss spinning disk confocal microscope with either Zeiss Plan-Apochromat 63X/1.2NA or 100X/1.4NA oil objectives using SlideBook 6.0 image acquisition and analysis software (Intelligent Imaging Innovation Inc). Anti-ATPB label was thresholded from 3D

images to measure total mitochondrial volume per cell or average volume of mitochondrial segment with SlideBook 6.0 image analysis software (LSI Imaging Core Facility, Life Sciences Institute, UBC, Canada).

To assess the impact of Gp78-dependent basal mitophagy on mitochondrial health and mitochondrial ROS, cells were plated in an ibidi chamber for 24 h. Cells were then transiently transfected, as indicated, with siRNA targeting ATG5 or Gp78 for 48 h and labelled with either the mitochondrial health sensor dye MitoView 633 or the mitochondrial ROS dye MitoSOX, at concentrations of 50 nM and 2.5 µM, respectively, for 30 min, washed 3X with warm PBS and incubated in Molecular Probes Live Cell Imaging Solution. Alternatively, cells were treated with CCCP for 4 h and then labeled with MitoView 633 for 30 min. Live-cell imaging was performed at 37ºC with a Leica TCS SP8 confocal microscope with a 100×/1.40 Oil HC PL APO CS2 objective (Leica, Wetzlar, Germany) equipped with a white light laser, HyD detectors, environmental chamber and Leica Application Suite X (LAS X) software (LSI Imaging Core Facility, Life Sciences Institute, UBC, Canada). Images were analyzed using ImageJ software to identify integrated densities of mitochondrial objects as well as the total area of the mitochondrial label, per cell. Integrated density per mitochondrial object reports specifically on dye intensity within individual mitochondria or mitochondrial segments and is therefore not impacted by varied mitochondrial content per cell.

Mitophagic flux assays

To study mitophagic flux in HT-1080 or Gp78 CRISPR/Cas9 knockout (g1-4, g2-41) cells by Western blot, early passage cells (420,000 cells per well) were plated in six well plates for 20 h, then washed with 1X PBS and treated with DMSO or CCCP in regular medium or medium lacking serum for 4 h. For each treatment, cells were challenged with 100 nM of BafA1 (Sigma) for 0, 30, 60 or 120 min prior to the end of the 4-h incubation period. Incubation was stopped by washing cells with ice-cold 1X PBS; cells were then harvested on ice lysed with M2-Lysis buffer [76] supplemented with phosphatase and protease inhibitors tablets (Roche), and lysates ran on 15% SDS-PAGE at constant voltage (75 V for fifteen minutes followed by 90 V for 2 h). Separated proteins were electrotransferred onto 0.2 µ pore size PVDF membrane (BioRad), fixed with 0.1% glutaraldehyde in PBST (0.2%) for 30 min, blocked with 5% milk in PBST and immunoprobed for LC3B-I and II and β-Actin. LC3B-II and β-actin bands were quantified by densitometry using ImageJ software, normalized and statistically analyzed.

To monitor mitophagic flux with mito-Keima, HT-1080 and Gp78 CRISPR/Cas9 knockout g2-41 cells (8,000 cells per well) were plated in an ibidi chamber for 24 h and then

transfected with mito-Keima plasmid [50] using Effectene transfection reagent (301425, Qiagen, USA). After 24 h, cells were washed with PBS and treated with DMSO or CCCP in regular medium. Following a 24 h incubation, the cells were washed 3X with PBS and then incubated in Live Cell Imaging Solution supplemented with 10% FBS, L-glutamine, D-glucose, and MEM Non-Essential Amino Acids Solution prior to imaging on a Leica TCS SP8 confocal microscope equipped with a 100x/1.40 Oil HC PL APO CS2 objective (Leica, Wetzlar, Germany), white light laser and HyD detectors (Leica, Wetzlar, Germany) (LSI Imaging Core Facility, Life Sciences Institute, UBC, Canada). mito-Keima in a neutral pH environment was detected by excitation at 470 nm and in an acidic environment by excitation at 561 nm. The HyD detector was open from 592 to 740 nm and equipped with a time gate limiting detection from 0.3 ns to 6.5 ns after laser activation. To quantify the presence of mitolysosomes, the fluorescent images were loaded into FIJI with the mito-QC Counter macro installed [51]. Settings (Radius for smoothing = 2.5, Ratio threshold = 1.6, Red channel threshold = 3.2) for ratio analysis were determined to report most accurately on mitolysosome expression across all data sets. For some images, large numbers of spots were detected that did not correspond to observed mitolysosomes. For consistency, the two images presenting the largest number of mitolysosomes per group were removed from the analysis.

To monitor autophagic flux with tfLC3, stably transfected HT-1080 and Gp78 CRISPR/Cas9 knockout g2-41 cells were plated overnight and then treated with either DMSO or CCCP for 4 h with or without 100 nM BafA1 for the final 2 h of the incubation period. Mitochondria were labelled with MitoTracker Deep Red FM half an hour prior to the end of the total incubation period. After incubation, cells were gently washed 3X with warm PBS and then incubated in warm Live Cell Imaging Solution just prior to image acquisition. Live-cell imaging was performed using Leica TCS SP8 confocal microscope with a $100 \times /1.40$ Oil HC PL APO CS2 objective (Leica, Wetzlar, Germany) equipped with a white light laser, HyD detectors, and Leica Application Suite X (LAS X) software (LSI Imaging Core Facility, Life Sciences Institute, UBC, Canada). Image acquisition was performed in a temperature-controlled system set to 37 °C.

For time lapse imaging, HT-1080 cells expressing tfLC3 were plated in ibidi chambers in Molecular Probes Live Cell Imaging Solution supplemented with 10% FBS, L-glutamine, D-glucose, and MEM Non-Essential Amino Acids Solution and labeled with MitoView 633 prior to imaging at 37ºC with the 100X/NA 1.45 PL APO objective (Zeiss) of a 3i Yokogawa X1 spinning disk confocal (LSI Imaging Core Facility, Life Sciences Institute, UBC, Canada). Image stacks of 7 images with a 500 nm Z spacing were acquired every minute for 40 min with a QuantEM

512SC Photometrics camera. Average intensity of MitoView 633 positive pixels overlapping each GFP-mRFP-positive tfLC3 puncta was assessed relative to average intensity of all MitoView 633-positive pixels in either the adjacent segmented mitochondria or in the cell.

tfLC3 spot detection analysis (SPECHT)

To identify tfLC3 labeled autophagic vacuoles (autophagosomes), we applied the SPECHT object detection method, that is consistent across channels and robust to intensity variations [45]. SPECHT evolved from the ERGO software for density detection in single molecule localization microscopy [77] and accepts as input a confocal image and produces, for each channel, a binary mask of detected fluorescent marker concentrations (spots or puncta). SPECHT leverages the Laplacian-of-Gaussian (LoG) object detection method, but ensures detection is adaptive to the image intensity distribution by computing an automatic threshold to postprocess LoG detected objects. The user can express a preference for recall or precision, which SPECHT then translates into channel/image specific threshold values. This preference is referred to in this manuscript as 'z-value'. A higher value increases precision, at the cost of recall. A lower value can result in higher recall, at cost of precision. To ensure no artificial objects are introduced, the isotropic Gaussian std. dev. was set to round(precision/2) = 3 pixels (pixel size = 56.6 nm). Objects with area smaller than 25 pixels were removed to avoid false counting of artifacts below the precision limit of the acquisition. Distances between objects were measured using Euclidean distance (pixels) between the closest edges of nearest objects. Puncta within 5 pixels (ceil(precision)) of mitochondria (i.e., the resolution limit of ~ 250 nm) cannot be distinguished from overlapping puncta and were thus counted as overlapping. The area of objects is represented by pixel mask counting. When a red mRFP and green GFP object (puncta) shared a non-zero intersection, the union of the red-green overlapping puncta were considered to correspond to early, neutral pH autophagosomes. Colocalized GFP-mRFP tfLC3 puncta upon BafA1 treatment encompass acidic autophagolysosomes and an increase in GFP-mRFP tfLC3 puncta following BafA1 treatment is a measure of autophagic flux. We also quantified the number of BafA1-induced GFP-mRFP overlapping tfLC3 puncta within 5 pixels of mitochondria.

To ensure single cell analysis, ROIs encompassing complete, individual cells within the field of view were manually segmented (Fig. 6). While this was feasible for the single time point analysis, to analyze moving cells in the time lapse series (Fig. 8), we therefore added an automated preprocessing stage to obtain cell segmentation masks. Input to SPECHT was a sequence of 2D images (1 Z-slice), 3 channels per timepoint. We recover the outline by applying a median filter (window

sizes 3×3, 5×5, 9×9) after filtering out the 90% intensity distribution quantile, binarizing the resulting image, and detecting disjointed objects separated by black (filtered) background using the connected components algorithm, such that the sole complete cell will be the largest object. To accommodate the highly fluctuating intensity distribution of live cell imaging over time, we enable SPECHT's autotuning mode configured to recover all possible objects (recall/precision ratio = 3.75). To prevent inclusion of false positives we: (1) compute the effect size (Cohen's d) of its intensity distribution with respect to that of the cell and discard any object with a negative effect size; (2) we use the heuristic that the local maxima contained within each detected object, should be a statistical outlier with respect to the overall intensity distribution (Q3 + 1.5 IQR, respectively, 3rd quartile and interquartile range) and discard objects that have a maximum intensity that is not at the extremum of the intensity distribution; (3) objects of area smaller or equal to 4 pixels are discarded, as they cannot be shown to be observable under the precision of the system (2 pixels). To ensure we do not compromise objects at the cell edge we widen the cell mask by a dilation operation 4 times ($2 \times$ system precision of 2 pixels). A closing operation ensures no holes are left in the cell mask should one channel have no or weak labelling in part of the resulting mask. To ensure our segmentation is valid, without the user having to screen each image, we test that the cell mask is consistent across channels. In addition, we disregard processing of any image where the cell mask touches the border of the image. The combination of high recall followed by high precision filtering, ensures a balanced, robust automatic pipeline for object detection designed for the live cell imaging data. For each GFP-mRFP overlapping spot (C12), we compute the mean mitochondria intensity, it overlaps relative to the mean intensity of the associated mitochondria segment as well as the mean intensity of all mitochondria segments in each given 2D image (C). We then compute a box plot of ratios 1 and 2 for all C12 objects, for each cell (Fig. 8), where each cell is represented by 7 2D images (per Z-slice), over 40 timepoints. Output is saved in csv files for statistical analysis and post-processing. The processing code is released under open source (https://github.com/bencardoen/SPECHT.jl, Affero GPLv3).

Subcutaneous xenograft tumor modeling

Disease modeling xenograft animal experiments were performed in collaboration with Investigational Drug Program located in BCCRC facility (Vancouver, Canada) following approved animal protocols and AICC guidelines. Briefly, HT-1080 and Gp78 KO Crispr clones were washed briefly one time with Hanks Balanced Salt Solution w/o Ca, Mg, trypsinized (0.25% trypsin with EDTA 4Na), neutralized with fresh growth medium and checked for viability and counted using Cellometer Auto T4. Using 27- or 28-guage needles,

1×10^6 cells in 50 μL volume were subcutaneously injected into the lower back area of at least six Rag2 immune compromised female mice per cell line. Post-injection, animals were monitored for body weight, appetite and behavioural changes as well as tumor development $3 \times$ weekly for at least 6 weeks or until a human endpoint was reached at 800 mm³. Animals were terminated (isoflurane overdose followed by CO_2 asphyxiation) and a necropsy performed to assess other signs of toxicity, examining the following organs: liver, gall bladder, spleen, lung, kidney, heart, intestine, lymph nodes and bladder. Harvested xenograft tumors were fixed in 10% buffered formalin for 24–48 h minimum before switching to 70% ethanol. Xenograft tumors were processed, paraffin embedded, sectioned and stained for H&E, TUNEL; immune labelled for mitochondria (ab92824) and Ki67 as proliferation marker by Wax-It Histology (UBC, Vancouver, Canada). Slides were scanned on a digital slide scanner from 3DHistec (LSI-UBC), analyzed using CaseViewer and ImageJ, and quantified on Graphpad Prism by performing one-way ANOVA statistical analysis.

Gene expression profiling interactive analysis (GEPIA) for cancer expression comparisons

Gene expression comparisons in cancer types were generated using GEPIA bioinformatics tool (http://gepia.cancer-pku.cn/about.html). Gene expression was denoted by transcripts per million (TPM) and were compared by generating a heatmap across various mitophagy regulators. Furthermore, gene expression of AMFR (Gp78) in various cancers was compared between tumor and matched normal TCGA and GTEx samples. TPM is displayed using log-scaling ($\log_2(TPM + 1)$). Significant expression between tumor and normal samples is performed using ANOVA with *$p < 0.01$).

Statistical analyses

One-way ANOVA with Dunnett's multiple comparison test was used for both the fixed and live-cell ROS experiments. One-way ANOVA with Tukey's multiple comparison test was used for the live cell tfLC3 flux, the mitoKeima experiments, the spinning disk mitochondrial volume experiments and the Western blot flux experiments and the xenograft tumor staining experiments. A two-tailed t test was applied for the siATG5 and protein expression blots. Statistical analyses were performed using GraphPad Prism 6.0 software.

Declarations

Conflict of interest The authors have no competing interests to disclose.

References

1. Zimmermann M, Reichert AS (2017) How to get rid of mitochondria: crosstalk and regulation of multiple mitophagy pathways. Biol Chem 399(1):29–45

2. Drake LE et al (2017) Expanding perspectives on the significance of mitophagy in cancer. Semin Cancer Biol 47:110–124

3. Harper JW, Ordureau A, Heo JM (2018) Building and decoding ubiquitin chains for mitophagy. Nat Rev Mol Cell Biol 19(2):93–108

4. Springer MZ, Macleod KF (2016) In brief: mitophagy: mechanisms and role in human disease. J Pathol 240(3):253–255

5. Gorrini C, Harris IS, Mak TW (2013) Modulation of oxidative stress as an anticancer strategy. Nat Rev Drug Discov 12(12):931–947

6. Murphy MP (2009) How mitochondria produce reactive oxygen species. Biochem J 417(1):1–13

7. Kalyanaraman B et al (2018) A review of the basics of mitochondrial bioenergetics, metabolism, and related signaling pathways in cancer cells: Therapeutic targeting of tumor mitochondria with lipophilic cationic compounds. Redox Biol 14:316–327

8. Wong HS et al (2017) Production of superoxide and hydrogen peroxide from specific mitochondrial sites under different bioenergetic conditions. J Biol Chem 292(41):16804–16809

9. Srinivas US et al (2019) ROS and the DNA damage response in cancer. Redox Biol 25:101084

10. Aggarwal V et al (2019) Role of reactive oxygen species in cancer progression: molecular mechanisms and recent advancements. Biomolecules 9(11):735

11. Mathew R, White E (2011) Autophagy, stress, and cancer metabolism: what doesn't kill you makes you stronger. Cold Spring Harb Symp Quant Biol 76:389–396

12. Poillet-Perez L et al (2015) Interplay between ROS and autophagy in cancer cells, from tumor initiation to cancer therapy. Redox Biol 4:184–192

13. Zhang H et al (2008) Mitochondrial autophagy is an HIF-1-dependent adaptive metabolic response to hypoxia. J Biol Chem 283(16):10892–10903

14. Zhang J, Ney PA (2009) Role of BNIP3 and NIX in cell death, autophagy, and mitophagy. Cell Death Differ 16(7):939–946

15. Schofield JH, Schafer ZT (2021) Mitochondrial reactive oxygen species and mitophagy: a complex and nuanced relationship. Antioxid Redox Signal 34(7):517–530

16. Pickrell AM, Youle RJ (2015) The roles of PINK1, parkin, and mitochondrial fidelity in Parkinson's disease. Neuron 85(2):257–273

17. Ordureau A et al (2015) Defining roles of PARKIN and ubiquitin phosphorylation by PINK1 in mitochondrial quality control using a ubiquitin replacement strategy. Proc Natl Acad Sci U S A 112(21):6637–6642

18. Lazarou M et al (2015) The ubiquitin kinase PINK1 recruits autophagy receptors to induce mitophagy. Nature 524(7565):309–314

19. Sekine S, Youle RJ (2018) PINK1 import regulation; a fine system to convey mitochondrial stress to the cytosol. BMC Biol 16(1):2

20. Xiao B et al (2017) Reactive oxygen species trigger Parkin/PINK1 pathway-dependent mitophagy by inducing mitochondrial recruitment of Parkin. J Biol Chem 292(40):16697–16708

21. Weidberg H, Shvets E, Elazar Z (2011) Biogenesis and cargo selectivity of autophagosomes. Annu Rev Biochem 80(1):125–156

22. Huynh DP et al (2001) Differential expression and tissue distribution of parkin isoforms during mouse development. Brain Res Dev Brain Res 130(2):173–181

23. McWilliams TG et al (2018) Basal mitophagy occurs independently of PINK1 in mouse tissues of high metabolic demand. Cell Metab 27(2):439–449

24. Villa E et al (2017) Parkin-independent mitophagy controls chemotherapeutic response in cancer cells. Cell Rep 20(12):2846–2859 (**e5**)

25. Narendra D et al (2008) Parkin is recruited selectively to impaired mitochondria and promotes their autophagy. J Cell Biol 183(5):795–803

26. Narendra DP et al (2010) PINK1 is selectively stabilized on impaired mitochondria to activate Parkin. PLoS Biol 8(1):e1000298

27. Aerts L et al (2015) PINK1 kinase catalytic activity is regulated by phosphorylation on serines 228 and 402. J Biol Chem 290(5):2798–2811

28. Kondapalli C et al (2012) PINK1 is activated by mitochondrial membrane potential depolarization and stimulates Parkin E3 ligase activity by phosphorylating serine 65. Open Biol 2(5):120080

29. Lee JJ et al (2018) Basal mitophagy is widespread in drosophila but minimally affected by loss of pink1 or parkin. J Cell Biol 217(5):1613–1622

30. Tang F et al (2011) RNF185, a novel mitochondrial ubiquitin E3 ligase, regulates autophagy through interaction with BNIP1. PLoS ONE 6(9):e24367

31. Di Rita A et al (2018) HUWE1 E3 ligase promotes PINK1/PARKIN-independent mitophagy by regulating AMBRA1 activation via IKKα. Nat Commun 9(1):3755

32. Rojansky R, Cha MY, Chan DC (2016) Elimination of paternal mitochondria in mouse embryos occurs through autophagic degradation dependent on PARKIN and MUL1. Elife 5:17896

33. Yun J et al (2014) MUL1 acts in parallel to the PINK1/parkin pathway in regulating mitofusin and compensates for loss of PINK1/parkin. Elife 3:e01958

34. Fu M et al (2013) Regulation of mitophagy by the Gp78 E3 ubiquitin ligase. Mol Biol Cell 24(8):1153–1162

35. Orvedahl A et al (2011) Image-based genome-wide siRNA screen identifies selective autophagy factors. Nature 480(7375):113–117

36. Park S et al (2014) Choline dehydrogenase interacts with SQSTM1/p62 to recruit LC3 and stimulate mitophagy. Autophagy 10(11):1906–1920

37. Szargel R et al (2016) The PINK1, synphilin-1 and SIAH-1 complex constitutes a novel mitophagy pathway. Hum Mol Genet 25(16):3476–3490

38. Fang S et al (2001) The tumor autocrine motility factor receptor, gp78, is a ubiquitin protein ligase implicated in degradation from the endoplasmic reticulum. Proc Natl Acad Sci U S A 98(25):14422–14427

39. Christianson JC et al (2011) Defining human ERAD networks through an integrative mapping strategy. Nat Cell Biol 14(1):93–105

40. Zhang T et al (2015) Gp78, an E3 ubiquitin ligase acts as a gatekeeper suppressing nonalcoholic steatohepatitis (NASH) and liver cancer. PLoS ONE 10(3):e0118448

41. Tsai YC et al (2007) The ubiquitin ligase gp78 promotes sarcoma metastasis by targeting KAI1 for degradation. Nat Med 13(12):1504–1509

42. Mukherjee R et al (2019) Calmodulin regulates MGRN1-GP78 interaction mediated ubiquitin proteasomal degradation system. FASEB J 33(2):1927–1945

43. Mukherjee R, Chakrabarti O (2016) Ubiquitin-mediated regulation of the E3 ligase GP78 by MGRN1 in trans affects mitochondrial homeostasis. J Cell Sci 129(4):757–773

44. Mookherjee D et al (2021) RETREG1/FAM134B mediated autophagosomal degradation of AMFR/GP78 and OPA1 -a dual organellar turnover mechanism. Autophagy 17(7):1729–1752

45. Cardoen B et al (2021) Specht: UNSUPERVISED Probabilistic multiple instance labelling of objects in biomedical images enables characterization of Transition dynamics in macromolecular structure and disease progression. PLOS One (in press)

46. St-Pierre P et al (2012) Peripheral endoplasmic reticulum localization of the Gp78 ubiquitin ligase activity. J Cell Sci 125(Pt 7):1727–1737

47. Wang PT et al (2015) Distinct mechanisms controlling rough and smooth endoplasmic reticulum contacts with mitochondria. J Cell Sci 128(15):2759–2765

48. Fu M et al (2011) Autocrine motility factor/phosphoglucose isomerase regulates ER stress and cell death through control of ER calcium release. Cell Death Differ 18(6):1057–1070

49. Shankar J et al (2013) Raft endocytosis of AMF regulates mitochondrial dynamics through Rac1 signaling and the Gp78 ubiquitin ligase. J Cell Sci 126(Pt 15):3295–3304

50. Katayama H et al (2011) A sensitive and quantitative technique for detecting autophagic events based on lysosomal delivery. Chem Biol 18(8):1042–1052

51. Montava-Garriga L et al (2020) Semi-automated quantitation of mitophagy in cells and tissues. Mech Ageing Dev 185:111196–111196

52. Gomez-Sanchez R et al (2015) Routine Western blot to check autophagic flux: cautions and recommendations. Anal Biochem 477:13–20

53. du Toit A et al (2018) Measuring autophagosome flux. Autophagy 14(6):1060–1071

54. Kimura S, Noda T, Yoshimori T (2007) Dissection of the autophagosome maturation process by a novel reporter protein, tandem fluorescent-tagged LC3. Autophagy 3(5):452–460

55. Katayama H et al (2008) GFP-like proteins stably accumulate in lysosomes. Cell Struct Funct 33(1):1–12

56. Barth S, Glick D, Macleod KF (2010) Autophagy: assays and artifacts. J Pathol 221(2):117–124

57. Klionsky DJ et al (2016) Guidelines for the use and interpretation of assays for monitoring autophagy (3rd edition). Autophagy 12(1):1–222

58. Rubinsztein DC, Shpilka T, Elazar Z (2012) Mechanisms of autophagosome biogenesis. Curr Biol CB 22(1):R29–R34

59. Poole LP, Macleod KF (2021) Mitophagy in tumorigenesis and metastasis. Cell Mol Life Sci 78(8):3817–3851

60. Chino H et al (2019) Intrinsically disordered protein TEX264 mediates ER-phagy. Mol Cell 74(5):909–921 (e6)

61. Singh R et al (2009) Autophagy regulates lipid metabolism. Nature 458(7242):1131–1135

62. Delorme-Axford E, Popelka H, Klionsky DJ (2019) TEX264 is a major receptor for mammalian reticulophagy. Autophagy 15(10):1677–1681

63. Marcassa E et al (2018) Dual role of USP30 in controlling basal pexophagy and mitophagy. EMBO Rep 19(7):e45595

64. Kurashige T et al (2019) Basal autophagy deficiency causes thyroid follicular epithelial cell death in mice. Endocrinology 160(9):2085–2092

65. Hara T et al (2006) Suppression of basal autophagy in neural cells causes neurodegenerative disease in mice. Nature 441(7095):885–889

66. Yang KC et al (2018) Evolution of tools and methods for monitoring autophagic flux in mammalian cells. Biochem Soc Trans 46(1):97–110

67. Kim YY et al (2019) Assessment of mitophagy in mt-Keima Drosophila revealed an essential role of the PINK1-Parkin pathway in mitophagy induction in vivo. FASEB J 33(9):9742–9751

68. McWilliams TG et al (2016) mito-QC illuminates mitophagy and mitochondrial architecture in vivo. J Cell Biol 214(3):333–345

69. Musiwaro P et al (2013) Characteristics and requirements of basal autophagy in HEK 293 cells. Autophagy 9(9):1407–1417

70. McWilliams TG et al (2019) A comparative map of macroautophagy and mitophagy in the vertebrate eye. Autophagy 15(7):1296–1308

71. Kirtonia A, Sethi G, Garg M (2020) The multifaceted role of reactive oxygen species in tumorigenesis. Cell Mol Life Sci 77(22):4459–4483

72. Chourasia AH et al (2015) Mitophagy defects arising from BNip3 loss promote mammary tumor progression to metastasis. EMBO Rep 16(9):1145–1163

73. Tracy K et al (2007) BNIP3 is an RB/E2F target gene required for hypoxia-induced autophagy. Mol Cell Biol 27(17):6229–6242

74. Joshi B, Li L, Nabi IR (2010) A role for KAI1 in promotion of cell proliferation and mammary gland hyperplasia by the gp78 ubiquitin ligase. J Biol Chem 285(12):8830–8839

75. Singhal SK et al. (2022) Protein expression of the gp78 E3 ligase predicts poor breast cancer outcome based on race. JCI Insight 7(13)

76. Joshi B et al (2008) Phosphorylated caveolin-1 regulates Rho/ROCK-dependent focal adhesion dynamics and tumor cell migration and invasion. Cancer Res 68(20):8210–8220

77. Cardoen B et al (2020) ERGO: efficient recurrent graph optimized emitter density estimation in single molecule localization microscopy. IEEE Trans Med Imaging 39(6):1942–1956